



HAL
open science

Fossil seamount in southeast Zagros records intraoceanic arc to back-arc transition: New constraints for the evolution of the Neotethys

Guillaume Bonnet, Philippe Agard, Hubert Whitechurch, Marc Fournier, Samuel Angiboust, Benoît Caron, Jafar Omrani

► To cite this version:

Guillaume Bonnet, Philippe Agard, Hubert Whitechurch, Marc Fournier, Samuel Angiboust, et al.. Fossil seamount in southeast Zagros records intraoceanic arc to back-arc transition: New constraints for the evolution of the Neotethys. *Gondwana Research*, 2020, 81, pp.423-444. 10.1016/j.gr.2019.10.019 . hal-03014574

HAL Id: hal-03014574

<https://hal.sorbonne-universite.fr/hal-03014574v1>

Submitted on 12 Nov 2024

HAL is a multi-disciplinary open access archive for the deposit and dissemination of scientific research documents, whether they are published or not. The documents may come from teaching and research institutions in France or abroad, or from public or private research centers.

L'archive ouverte pluridisciplinaire **HAL**, est destinée au dépôt et à la diffusion de documents scientifiques de niveau recherche, publiés ou non, émanant des établissements d'enseignement et de recherche français ou étrangers, des laboratoires publics ou privés.



Distributed under a Creative Commons Attribution - NonCommercial - NoDerivatives 4.0 International License

1
2
3
4
5
6
7
8
9
10
11
12
13
14
15
16
17
18
19
20
21
22
23
24
25
26
27
28
29
30
31
32

**Fossil seamount in southeast Zagros records intraoceanic arc to back-arc transition:
new constraints for the evolution of the Neotethys**

Bonnet, G.^{a,b,*}, Agard, P.^a, Whitechurch, H.^c, Fournier, M.^a, Angiboust, S.^e, Caron, B.^a, Omrani, J.^e

^a Sorbonne Université, CNRS-INSU, Institut des Sciences de la Terre de Paris, IStEP UMR 7193, F-75005 Paris, France

^b now at: Earth Research Institute and Department of Earth Science, University of California, Santa Barbara, CA 93106, USA

^c Institut de Physique du Globe de Strasbourg, EOST-CNRS-UMR 7516, Université de Strasbourg, 67000 Strasbourg, France

^d Institut de Physique du Globe de Paris, Sorbonne Paris Cité, Université Paris Diderot, CNRS, F-75005 Paris, France

^e Geological Survey of Iran, Tehran, Iran

* Corresponding author: gbonnet01@gmail.com

Abstract

The Neotethys ocean is transiently involved in two subduction zones during the Late Cretaceous. While the Northern Neotethys subduction zone (below Eurasia) was active from the early Mesozoic until the Eocene, the intra-oceanic Southern Neotethys subduction zone only developed during the Late Cretaceous. We herein document, through a combination of structural, geochemical and geochronological data, the magmatic evolution of a Late Cretaceous supra-subduction ophiolite fragment of the Neotethys (the Siah Kuh massif, Southern Iran), now sandwiched in the Zagros suture zone. Results show that this ophiolite fragment — a subducted yet exceptionally well-preserved seamount — records an evolution from supra-subduction zone magmatism (including island arc tholeiites, boninites and calc-alkaline transitional magmatism) around 87 Ma, to MORB (from E-MORB to N-MORB) magmatism at 78 Ma, and potentially until 73 Ma. We conclude that this seamount initially formed in an arc context and represents either (i) a non-obducted remnant of the Oman ophiolite that experienced a longer-lived magmatic history (preferred hypothesis) or (ii) a

33 *piece from the forearc/frontal arc of the Northern margin of the Neotethys. Regardless of its*
34 *exact original location, the Siah Kuh seamount was later subducted in the Northern*
35 *Neotethys subduction zone.*

36

37

38

39

40

41 **1. Introduction**

42 Alike modern ocean floor, ophiolites exposed throughout the world span a range of
43 geochemical signatures, in part reflecting their diverse original tectonic setting: mid-ocean
44 ridges, ocean islands (hotspots), island arcs (Pearce, 2008). On modern ocean floor,
45 seamounts are defined as “geographically isolated topographic feature[s] on the seafloor
46 taller than 100 m, including ones whose summit regions may temporarily emerge above sea
47 level, but not including features that are located on continental shelves or that are part of
48 other major landmasses” (Staudigel et al., 2010). While the majority of these seamounts are
49 thought to have formed through hotspot-fed magmatism (and have ocean island basalt –
50 OIB – affinities, e.g. Hawaiian islands), many of them also form along ocean ridges (e.g. at
51 the East Pacific Rise, Batiza and Vanko, 1984; with mid-ocean ridge basalt – MORB –
52 affinities) and in volcanic arc contexts (e.g. Izu-Bonin arc system, Hochstaedter et al., 2001)
53 with island arc tholeiite – IAT – to calc-alkaline affinities).

54 Seamounts are however rarely preserved in the geological record of the ocean floor, i.e.
55 within ophiolitic material. Most of them indeed get subducted (Ranero and von Huene,
56 2000) with only fragments left over (Cloos, 1993), that may even not be recognized as such
57 (unless having an OIB-like signature; e.g. Hauff et al., 1997; John et al., 2010). A few
58 seamounts however escape subduction and are docked in accretionary wedges (e.g. Nicasio
59 Reservoir Terrane, Schnur and Gilbert, 2012) or are shallowly subducted and underplated,
60 but very few are exhumed almost intact. Notable exceptions are the late Paleozoic Anarak
61 and Kabudan seamounts (Bagheri and Stampfli, 2008; Central Iran) and the Mesozoic Snow
62 Mountain (MacPherson, 1983; Franciscan complex, USA), identified according to their
63 structure and OIB signatures.

64 In the Mesozoic realm of the Neotethys, the geological record is dominated by supra-
65 subduction zone (SSZ) ophiolites, that may represent either forearc ocean floor, oceanic arc
66 or back-arcs (Moghadam and Stern, 2015 and references therein). This preferential record is
67 consistent with the mechanism leading to the obduction of ophiolite, starting from intra-
68 oceanic subduction initiation (Agard et al., 2007; Boudier et al., 1988), forearc spreading
69 (Casey and Dewey, 1984) and leading to continental subduction below the newly formed
70 ophiolite (Searle et al., 2004). Small ocean basins formed in back-arc settings behind
71 continental stripes are also partly preserved during collision (e.g. Agard et al., 2011; Rossetti
72 et al., 2010).

73 These ophiolitic fragments therefore preserve essential information regarding subduction
74 processes and magmatic evolution on the seafloor. However (with the exception of the
75 extensively studied Semail ophiolite in Oman), most large-scale ophiolites or ophiolitic
76 “*mélanges*” exposed in the Zagros-Makran orogens are strongly dismembered (Burg, 2018;
77 Whitechurch et al., 2013).

78 This makes the recently discovered Siah Kuh seamount (Bonnet et al., 2019a) the ideal target
79 to study the continuous evolution and origin of magmatic activity in an ophiolite, with
80 implications for lithosphere formation, mantle heterogeneities and regional geodynamics.

81 This contribution therefore addresses three major questions:

- 82 (1) In the light of geochemical and geochronological data, what is the origin of the Siah
83 Kuh seamount (i.e., mid-ocean ridge seamount, hotspot/plume related, arc-related)?
- 84 (2) Does the Siah Kuh seamount preserve evidence for progressive changes in
85 magmatism and/or in the nature of the (mantle) source?
- 86 (3) Does this help constrain the former location of the seamount in the Neotethys
87 realm?

88 To that end, we herein present detailed petrological and geochemical data, i.e. bulk-rock
89 analyses of major, trace elements and Sr-Nd isotopes, as well as dating and Hf isotope
90 analysis of zircons from representative lithologies.

91

92

93 **2. Geological setting**

94 **2.1. Ocean-floor and arc preservation in the Iran-Oman Neotethys**

95 The Zagros-Makran orogen formed through the closure of an allegedly large oceanic basin,
96 the Neotethys ocean (probably larger than 1000 km, Agard et al., 2011; Barrier and
97 Vrielynck, 2008). Remnants of this basin are found in Oman (including the thoroughly
98 studied Semail ophiolite) and in Iran along two ophiolite belts: the Outer and Inner
99 Zagros/Makran ophiolite belts (McCall, 1997; Stöcklin, 1981; Fig. 1a).

100 In the Zagros, the Outer ophiolite belt, located along the Main Zagros Thrust (MZT) includes
101 the (relatively coherent) ophiolitic massifs of Khoy, Kermanshah, Neyriz and Hajiabad-
102 Esfandagheh (from Northwest to Southeast). The Hajiabad (Esfandagheh) ophiolitic
103 exposures (Fig. 1b) are associated with the only blueschist exposures in the Zagros, which
104 led Agard et al. (2006) to interpret the MZT as the Zagros Suture Zone. Dismembered pieces
105 of ophiolites are also found all along the MZT in the so-called “colored mélange” (Gansser,
106 1960).

107 All Zagros ophiolites display a large age spread (except the Neyriz ophiolite, where only Late
108 Cretaceous magmatism was described; Babaie et al., 2006; Lanphere and Pamić, 1983;
109 Monsef et al., 2018a), suggesting different stages of magmatic activity, notably during the
110 Triassic-Liassic and Late Cretaceous to Paleocene periods (Ao et al., 2016; Moghadam et al.,
111 2013b, 2017; Whitechurch et al., 2013). The Triassic-Liassic magmatism usually shows
112 alkaline to MORB signatures, whereas the Late Cretaceous one shows an SSZ signature (Ali et
113 al., 2012; Babaie et al., 2001; Khalatbari-Jafari et al., 2004; Moghadam et al., 2013b, 2014b;
114 Saccani et al., 2013; Whitechurch et al., 2013).

115 The Sanandaj-Sirjan Zone, to the North of the Zagros Suture Zone, is interpreted as a piece of
116 the Eurasian upper plate (e.g. Agard et al., 2011; Ghasemi and Talbot, 2006) that separates
117 the Outer Zagros ophiolite belt from the Inner Zagros ophiolite belt. This belt comprises
118 small dismembered ophiolitic massifs including the Nain, Dehshir, Shahr-e Babak and Baft
119 locations from Northwest to Southeast (abbreviated hereafter as “Nain-Baft”). The
120 magmatism within these units has strong SSZ signatures (Moghadam et al., 2009) and
121 occurred from 'mid' Cretaceous to early Paleocene (Arvin and Robinson, 1994; Moghadam et
122 al., 2013a, 2013c, 2010). Most authors separate the Outer and Inner ophiolite belts, the
123 former being a forearc of a northward-dipping subduction zone (responsible for the Zagros
124 blueschists), the latter being the coeval back-arc (e.g. Agard et al., 2011; Arvin and
125 Robinson, 1994; Moghadam et al., 2009), although some have proposed that both ophiolitic
126 belts belong to the same ophiolite (e.g. Moghadam et al., 2010).

127 McCall (1997) proposed a continuity between the Zagros and the Makran ophiolites. The
128 Outer (“Colored Mélange”) and Inner ophiolite belts are separated by the Bajgan-Durkan
129 complex, analogous to the Sanandaj-Sirjan zone. Cretaceous blueschist facies ophiolitic units
130 of the North Makran suture are however located to the north and structurally above all of
131 these units (Hunziker et al., 2017) and suggest a slightly different geological evolution than in
132 the Zagros. In spite of the scarcity of intact ophiolitic exposures in the continuity of the
133 Outer ophiolite belt, the study of dismembered ophiolites allowed the identification of Late
134 Cretaceous (possibly starting during Early Cretaceous) magmatism with dominant SSZ and
135 accessory MORB signatures (Saccani et al., 2018). Ophiolites in the Inner Makran ophiolite
136 belt, including the Band-e Zeyarat/Dar-e Anar, Ganj, Rameshk-Mokhtarabad, Fannuj-
137 Maskutan, Kahiri-Espakeh and Iranshahr ophiolitic massifs testify to an Early Cretaceous
138 magmatic stage, associated with alkaline (OIB) magmatism, and Late Cretaceous SSZ
139 magmatism (Burg, 2018; Ghazi et al., 2004; Kananian et al., 2001; Monsef et al., 2018b).
140 Across the Gulf of Oman, the Semail ophiolite is commonly regarded as having formed
141 during the Late Cretaceous (96-94 Ma; Goodenough et al., 2010; Rioux et al., 2013, 2012;
142 Warren et al., 2005), in a SSZ context with increasing maturity, yet never reaching a mature
143 arc stage (Alabaster et al., 1982; Godard et al., 2003).
144 Given the variety of Late Cretaceous ophiolitic remnants from the Neotethys, linking them to
145 a specific geodynamic context may prove difficult (see the schematic paleogeographical map
146 on Fig. 1c). Exceptional pieces of oceanic lithosphere like the Siah Kuh seamount may help
147 constraining the paleogeography of the Iran-Oman transect, with critical inference for
148 regional-scale geodynamics.

149

150 2.2. The Siah Kuh massif, an exhumed seamount

151 The Siah Kuh unit is a 18x12 kilometer-wide and >1.5 km-high coherent portion of ocean
152 floor (Fig. 2a,b) belonging to the Hajiabad ophiolite, close to the transition between Zagros
153 and Makran. At variance to earlier map reports (“colored mélange”, Azizan et al., 2007;
154 Madjidi et al., 1993; Nazemzadeh et al., 2007), this unit is a coherent magmatic unit with
155 some sediments and subordinate serpentinite only. It is tectonically overlain by blueschist
156 facies units metamorphosed during Late Cretaceous (Agard et al., 2006; Angiboust et al.,
157 2016; Moghadam et al., 2017; Monié and Agard, 2009; Sabzehei, 1974) and by rocks of the
158 Sanandaj-Sirjan zone (locally represented by the Sikhoran ultramafic-mafic complex (itself

159 capped by metasediments of the Sargaz-Abshur unit, Ahmadipour et al., 2003; Ghasemi et
160 al., 2002). The so-called Siah Kuh granitoids (Arvin et al., 2007) dated to 200 Ma, are located
161 to the North and thrust upon the Siah Kuh unit of this paper, but are not part of it.

162 The architecture of the Siah Kuh unit is summed up on Fig. 2 (after Bonnet et al., 2019). The
163 Siah Kuh unit is separated into two sub-units (A and B) by a major, km-scale thrust. The A
164 unit is characterized by a magmatic core (A_1) stratigraphically overlain by reef limestone and
165 pelagic sediments, upon which new lavas are erupted (Fig. 2c and Fig. 3a,b).

166 The core of the A unit (A_1) is made of pillow basalts (Fig. 3c) and breccias, intruded by felsic
167 magmatic rocks (Fig. 3d). Moghadam et al. (2013b) reported boninite lavas in this part of the
168 Siah Kuh unit (although the location of these samples is approximate – near the Avenân
169 village, see Fig. 2a – they are unambiguously within and close to the top of the A_1 unit). The
170 felsic intrusions are associated with rhyo-dacitic lava flows on top of the basalts.

171 The lava flows of the core A_1 unit are stratigraphically overlain by up to 400 meters of
172 deepening-up oceanic sediments (Fig. 3a,b,d). The basal sediment is reef to lagoon-like with
173 remains of foraminifera, urchin spines and gastropods (Bonnet et al., 2019a), but is locally
174 absent. Deeper sediments constituted of tuffaceous sandstone, clays, radiolarite and pelagic
175 limestone are deposited above this shallow limestone, all of which are locally infiltrated by
176 felsic sub-volcanic material. These sediments are assumed to be of Campanian to
177 Maastrichtian age in former studies (84-66 Ma; Sabzehei, 1974).

178 Up to 1 km-thick pillow basalts and basaltic flows (units A_1 - A_2 - A_3 - A_4 of Fig. 2a) have been
179 erupted directly on top of the sediments (Fig. 3a,b). While the contact between the A_1 unit
180 and A_1 - A_2 - A_3 - A_4 was very often reworked by faults parallel to the sedimentary layer, the
181 original unfaulted, stratigraphic contact is preserved in some places (such as between A_1 and
182 A_1 , Fig. 2a). This large volume of lavas, marking the resumption of volcanic activity after
183 some period of magmatic inactivity, is described as a “rejuvenation event” in Bonnet et al.
184 (2019). We later separate this rejuvenation event in “early-stage rejuvenation” for the lavas
185 located just above the sediments and “late-stage” for lavas higher in the sequence. As
186 pointed out by Bonnet et al. (2019), the A unit as a whole has all the characteristics of a
187 seamount (i.e. a bathymetric anomaly on the seafloor).

188 The second sub-unit (Unit B) has a serpentized ultramafic base intruded by an anorthosite
189 dike (Fig. 3e) and rodingite pods. A large volume of gabbro overlies the ultramafics, with
190 fining-upwards grain size. A 300 m-thick body of felsic volcanics overlain by a thin and very

191 discontinuous layer of pelagic sediments is intercalated in coarse-grained gabbros and
192 diabase (Fig. 3f). In the southern part of the B unit, gabbros are overlain by basalts. The
193 abundance of felsic rocks (rare in ophiolitic rocks from adjacent areas) and sedimentary
194 intercalations that can be correlated with the structure of the A unit suggest that this unit
195 could be a lateral equivalent of the seamount core.

196 The whole Siah Kuh seamount was then subducted to ~30 km depth, as attested by very
197 incipient high-pressure metamorphism marked by lawsonite and aragonite crystallization
198 (e.g. Fig. 4d,e). It was subsequently exhumed as an intact piece, with limited subduction-
199 related deformation (these aspects, beyond the scope of the present study, are detailed in
200 Bonnet et al., 2019a, 2019b).

201

202 **3. Sampling and analytical methods**

203 Approximately 100 samples of magmatic rocks and serpentinized ultramafics were collected
204 in different units of Siah Kuh, including the core of the seamount, the early and late stages of
205 the magmatic rejuvenation, gabbros, diabase and basalt of the B unit, as well as felsic
206 volcanics and subvolcanics. After examination of thin sections, 36 samples were selected for
207 detailed analyses (Table 1). The precise GPS location of each sample is given in
208 Supplementary Material S1.

209 An aliquot of each magmatic sample (31 samples) was crushed and powdered for 30 minutes
210 with an electric mortar in agate to avoid contamination. These samples were finely crushed
211 to <2 μm grains for major, trace and Sr-Nd isotopes analyses. About 4 g of each sample was
212 dried at 110°C in an alumina crucible and heated twice for one hour to 1000°C and
213 reweighted for loss on ignition calculation.

214 Major elements analyses were performed at ALIPP6 (Sorbonne Université) by ICP-OES
215 spectroscopy (with an Agilent 5100 SVDV ICP-OES) after dissolution at 80°C with HNO_3 and
216 HF and neutralization with $\text{B}(\text{OH})_3$. Trace element analyses were also performed at ALIPP6
217 (Sorbonne Université) through QQQ-ICP-MS spectroscopy (using an Agilent 8800 ICP-QQQ-
218 MS) after dissolution at 80°C with HNO_3 and HF and neutralization with HNO_3 and H_3BO_3 .

219 Detailed analyses are provided in Supplementary Material S2. Geochemical data were
220 normalized to the primitive mantle values and chondrite values (Sun and McDonough,
221 1989).

222 12 samples were selected for bulk rock Sr-Nd isotopic analyses (performed at SARM, Nancy).
223 ϵNd_i and $^{87}\text{Sr}/^{86}\text{Sr}(t)$ values were calculated on the basis of their expected ages
224 (Supplementary Material S3). These corrections change the ϵNd and $^{87}\text{Sr}/^{86}\text{Sr}$ values by a
225 maximum of 0.7 and 0.00001, respectively.

226 Clinopyroxene and spinel compositions of 10 basaltic samples and 5 serpentinites have been
227 analyzed using a Cameca SX100 electron microprobe (15 kV, 10 nA, 1 μm spot, WDS) at
228 CAMPARIS (Sorbonne Université), with diopside (Si, Ca, Mg), orthoclase (K, Al), MnTiO_3 (Mn,
229 Ti), Fe_2O_3 (Fe) and albite (Na) as standards. The analyses were sorted and Fe^{3+}
230 concentrations were estimated using the method exposed by Droop (1987). Analyses are
231 provided in Supplementary Materials S4 and S5.

232 Four samples were coarsely crushed and zircon grains were separated for U-Pb dating and Hf
233 isotope analysis, using conventional heavy fraction and magnetic techniques. Zircon grains
234 were placed on epoxy mounts and then polished to expose their half-sections, which were
235 photographed under transmitted and reflected light using an optical microscope to reveal
236 internal cracks and mineral inclusions. Cathodoluminescence (CL) images of the zircon grains
237 were generated using a LEO1450VP scanning electron microscope (SEM) with an attached
238 Gatan MinCL detector at IGGCAS (Supplementary Material S6).

239 U-Pb dating and trace element analysis of zircons from 4 samples were simultaneously
240 conducted by LA-ICP-MS at the Wuhan SampleSolution Analytical Technology Co., Ltd.,
241 Wuhan, China. Detailed operating conditions for the laser ablation system and the ICP-MS
242 instrument and data reduction are the same as description by Zong et al. (2017). Laser
243 sampling was performed using a GeolasPro laser ablation system that consists of a
244 COMPexPro 102 ArF excimer laser (wavelength of 193 nm and maximum energy of 200 mJ)
245 and a MicroLas optical system, with a spot size of 32 μm . An Agilent 7700e ICP-MS
246 instrument was used to acquire ion-signal intensities. Helium was applied as a carrier gas.
247 Argon was used as the make-up gas and mixed with the carrier gas via a T-connector before
248 entering the ICP. A “wire” signal smoothing device is included in this laser ablation system
249 (Hu et al., 2015). Zircon 91500 and glass NIST610 were used as external standards for U-Pb
250 dating and trace element calibration, respectively. Each analysis incorporated a background
251 acquisition of approximately 20-30 s followed by 50 s of data acquisition from the sample.
252 An Excel-based software ICPMSDataCal was used to perform off-line selection and
253 integration of background and analyzed signals, time-drift correction and quantitative

254 calibration for trace element analysis and U-Pb dating (Liu et al., 2010, 2008). Common-Pb
255 correction was done using the method of Andersen (2002). Data reduction was carried out
256 using the Isoplot/Ex v. 2.49 programs (Ludwig, 2001). Analyses of reference zircon Plešovice
257 as an unknown give an accurate date within uncertainty (338.4 ± 1.9 Ma, compared to
258 337.13 ± 0.37 ; Sláma et al., 2008). U-Pb and trace element analyses of zircons are provided
259 in Supplementary Material S7, S8 and S9.

260 In-situ zircon Lu-Hf isotopic analyses were carried out using a Neptune MC-ICP-MS with an
261 ArF excimer laser ablation system. Hf isotopic analyses were obtained on the same zircon
262 grains that were previously analyzed for LA-ICP-MS U-Pb isotopes, with ablation pits of 32-65
263 μm in diameter and a laser repetition rate of 10 Hz with 100 mJ was used. Details of the
264 technique are described by Wu et al. (2006). Decay constant by Söderlund et al. (2004) and
265 present-day chondritic ratios by Bouvier et al. (2008) were adopted to calculate $\epsilon_{\text{Hf}}(t)$
266 values. The single stage model age (T_{DM}) was calculated by using the present-day depleted
267 mantle isotopic ratios (Supplementary Material S10, Vervoort and Blichert-Toft, 1999).

268

269 **4. Petrography**

270 A summary of the mineralogical assemblages is provided in Table 1. We report on Fig. 4
271 pictures of representative textures from mafic rocks in A (Fig. 4a-c), in B (Fig. 4d-f) and felsic
272 rocks in A (Fig. 4g) and B (Fig. 4h,i).

273

274 **Mafic lavas**

275 Mafic lavas are the main constituent of unit A and of the top of B (Fig. 2). They are all
276 basaltic, with clinopyroxene, plagioclase and Fe-Ti oxides in a glassy matrix (Fig. 4a-c,f). Most
277 samples show evidence of hydrothermal alteration, marked by the growth of secondary
278 phases. Pumpellyite, epidote and chlorite usually replace primary clinopyroxene and volcanic
279 glass, while primary plagioclase is often albitized. Quartz, calcite, epidote, prehnite, and
280 pumpellyite fill vesicles and veins that result from strong degassing of magmas during
281 eruption (eg. Fig. 4f). Green amphibole is found in one basalt. Clinopyroxene phenocrysts are
282 more frequent in the A_1 unit, but generally units cannot be distinguished solely based on
283 magmatic textures.

284 A few samples show crystallization of high-pressure minerals during subduction, such as
285 lawsonite and pumpellyite replacing plagioclase in one sample, or more frequently
286 aragonite-bearing veins (see Bonnet et al., 2019 for more details).

287

288 **Gabbros and diabase**

289 Gabbroic rocks are found within the B unit. They are mainly made of plagioclase surrounded
290 by clinopyroxene, with oxide and rare olivine. One sample (#1532) was recovered in a
291 sequence with strong grain size variations (potentially cumulitic). Poikilitic textures are
292 observed in the zones of smaller grain size (Fig. 4d). Hydrothermal minerals include
293 amphibole and chlorite replacing clinopyroxene and serpentine replacing rare olivine. High-
294 pressure metamorphism is common in these samples with lawsonite and pumpellyite
295 replacing plagioclase (Fig. 4d,e).

296

297 **Felsic lavas**

298 Felsic lavas in A are mainly rhyolites, with large hexagonal quartz crystals, crystals of
299 orthoclase and oxides in a glassy matrix (Fig. 4g). K-feldspar and glass are usually altered to
300 pumpellyite, epidote and chlorite. One rhyolite also contains aragonite and lawsonite in
301 veins.

302 Felsic lavas in B are dacitic, with abundant plagioclase, quartz and oxides in a glassy matrix
303 (Fig. 4e). Plagioclase is albitized and the glass is altered to epidote and chlorite during
304 hydrothermalism.

305

306 **Felsic intrusives**

307 Felsic intrusives are observed within the A units. They are composed of quartz, plagioclase
308 and K-feldspar. They are characterized by the crystallization of secondary epidote, possibly
309 replacing unidentified primary phases.

310

311 **Anorthosite**

312 One anorthosite dyke (#1720) was found in serpentinized ultramafics at the base of the B
313 unit. It is composed of 95% plagioclase, 4% titanite and contains some zircons (Fig. 4i).

314

315 **Ultramafic material**

316 Ultramafics are found within both the A and B units, and are close to 100% serpentinized
317 (chrysotile-lizardite, except for spinel that is generally preserved). One sample of
318 serpentinized ultramafics from the A unit is likely a former dunite with two generations of
319 Al-Cr-rich spinel distinguished by their color.

320 By contrast, ultramafics of the B unit more likely represents a former harzburgite or a
321 cumulate ultramafic sequence, with little-deformed patches of former olivines, and
322 abundant bastite replacing former pyroxene, whose cleavage is revealed by Fe-Ti oxides. A
323 chromitite pod within the ultramafics of the B unit is made of 90% of Cr-spinel and 10%
324 serpentine.

325 Spinel is the main aluminium-bearing phase in all ultramafic samples. All samples also have
326 secondary magnetite crystallization around serpentinized olivine domains.

327

328 **5. Bulk rock geochemistry**

329 The whole Siah Kuh volcanic sequence has been affected by hydrothermal alteration, as
330 shown by the widespread occurrence of secondary phases such as chlorite and pumpellyite
331 (e.g. Fig. 4f). This is further evidenced by addition of H₂O, as attested by the 0.9 to 8.5 wt.%
332 loss on ignition of the rocks (the loss on ignition may in part correspond to CO₂ loss, from
333 minor secondary carbonate vesicles). To avoid any bias due to major element mobilization
334 during hydrothermal alteration and/or high-pressure metamorphism, we only present
335 diagrams based on elements assumed to be immobile (see discussion in paragraph 9.1).
336 Immobile-element-based classifications of mafic rocks are shown on Fig. 5, trace element
337 spectra on Fig. 6 and trace-element based discrimination diagrams on Fig. 7.

338

339 **Core of the seamount (A₁)**

340 Mafic rocks from the core of the seamount plot in the subalkaline basaltic field in the Zr/Ti –
341 Nb/Y diagram (Pearce, 1996; Fig. 5a) and in the tholeiitic basalt to andesite fields in the Th –
342 Co diagram (Hastie et al., 2007; Fig. 5b). REE diagrams (Fig. 6a) show low LREE content
343 compared to MREE and HREE (with very low REE contents for two samples: <5*chondrite for
344 LREE and <8*chondrite for HREE). These rocks have trace element signatures very similar to
345 the lower V2 lavas from Oman (Alabaster et al., 1982; Godard et al., 2003; Kusano et al.,
346 2014). Multielementary spider diagrams (Fig. 6b) show strong Nb-Ta negative anomalies,
347 and small Ti negative anomalies. They plot in the IAT field on the Th/Yb – Nb/Yb (Pearce,

348 2008a; Fig. 7a), in the arc field of the V – Ti diagram (Shervais, 1982; Fig. 7b) and in the IAT
349 and calc-alkaline fields of the Th – Hf – Ta diagram (Wood, 1980; Fig. 7c). They range
350 between MORB and arc basalts in the Th/La – Sm/La diagram (Plank, 2005; Fig. 7d). One
351 sample (#1628) shows Th and LREE enrichment and plots in or close to the calc-alkaline field
352 of the former diagrams.

353

354 **Boninites**

355 Boninites from the core of Siah Kuh were not analyzed in this study, but we herein report
356 bulk-rock analyses by Moghadam et al. (2013b). They are classified as subalkaline basalts in
357 figure 5a, and as tholeiitic basalts to andesites in figure 5b. REE diagrams show strong
358 depletion in LREE compared to HREE (Fig. 6a). They are chemically very close to Oman
359 boninites (upper V2, Ishikawa et al., 2005, 2002; Kusano et al., 2014). They plot in the IAT
360 field in figure 7a and in the boninite field in figure 7b.

361

362 **Felsic rocks**

363 Felsic rocks plot in the subalkaline basaltic andesite/andesite field in figure 5a, except for
364 one sample in the dacite/rhyolite field (despite being petrographically dacites and rhyolites
365 or subvolcanic equivalents) and in the tholeiitic dacite/rhyolite field in figure 5b. No obvious
366 difference exists between the felsic rocks of the A₁ unit and those of the B unit (apart from a
367 smaller Ti negative anomaly in the latter). They have flat to slightly decreasing REE patterns,
368 with marked negative Eu anomaly (Fig. 6c). Multi-elementary spider diagrams show strong
369 Nb-Ta and Ti negative anomalies, and small Zr negative anomalies (Fig. 6d). They also plot in
370 the IAT fields in figures 7a and 7c (except for one sample plotting in the calc-alkaline field;
371 the use of those diagrams is however contested for felsic rocks; Pearce, 2008a). They mainly
372 plot as arc lavas in the Th/La – Sm/La diagrams, with higher Th/La ratios than other rocks.

373

374 **Early stage rejuvenation (A unit: A₁ and A₂)**

375 Lavas from the early rejuvenation stage plot as subalkaline in figure 5a, and as tholeiitic
376 basalts in figure 5b. They are enriched in LREE compared to HREE (Fig. 6e). Multi-elementary
377 spider diagrams show no significant HFSE negative anomaly (Fig. 6f). They plot in-between E-
378 MORB and N-MORB in figure 7a, and in the MORB – back-arc basalt field in figure 7b. They
379 are in the E-to-N-MORB transition zone of figure 7c, and are classified as MORB in figure 7d.

380

381 **Late stage rejuvenation (A unit: A₁' and A₄)**

382 Rocks from the late stage rejuvenated magmatism are classified as subalkaline basalts in
383 figure 5a and as tholeiitic basalts to andesites in figure 5b. They have bell-shaped REE
384 patterns with depletion in LREE and slight depletion in HREE compared to MREE (Fig. 6e).
385 Multi-elementary spider diagrams show very small Nb-Ta and Ti negative anomalies (Fig. 6f).
386 They plot close to N-MORB in figure 7a and in the MORB – back-arc basalt field of figure 7b.
387 They are classified as N-MORB in figure 7c, and as MORB (yet closer to the OIB field the the
388 early-stage rejuvenation lavas) in figure 7d.

389

390 **B unit diabases**

391 Samples from the base of the B unit are classified as subalkaline in figure 5a and as tholeiitic
392 basalts in figure 5b. They are enriched in LREE, but have almost flat MREE-HREE trend (Fig.
393 6g). Multi-elementary spider diagrams show small positive Nb-Ta anomalies but strong
394 negative Zr-Hf anomalies (Fig. 6h). They plot very close to E-MORB in figure 7a and in the
395 MORB-BABB field of figure 7b. They plot in the E-MORB to OIB basalt transition in figure 67c
396 and 7d.

397

398 **B unit basalts**

399 Basalts from the top of the B unit are classified as subalkaline basalts in figure 5a and as
400 tholeiitic basalts in figure 5b. They have again a flat, slightly bell-shaped REE patterns with a
401 small enrichment in MREE compared to LREE and HREE (Fig. 6g). Multi-elementary spider
402 diagrams show an insignificant negative Ti anomaly (Fig. 6h). They plot in-between the N-
403 and-E-MORB fields of figures 7a and 7c, in the MORB-BABB field of figure 7b, and in the
404 MORB field of figure 7d..

405

406 **Anorthosite**

407 Its REE pattern has high LREE to HREE ratio and a strong positive Eu anomaly, characteristic
408 of plagioclase (Fig. 6c). Multi-elementary spider diagrams show Zr-Hf and Ti negative
409 anomalies (Fig. 6d).

410

411 **Gabbros of the B unit**

412 Two gabbros within the B unit show very distinct geochemical signatures (Fig. 6g,h). One
413 (#1738) has a REE profile very similar to the diabase of the B unit, with similar positive Nb-Ta
414 positive anomalies and Zr-Hf negative anomalies but with a positive Ti anomaly. The other
415 one (#1532, dated) has enriched MREE and HREE compared to LREE, with a positive Eu
416 anomaly and small negative Ti anomaly. The later resembles the N-MORB-like basalts from
417 the top of the B unit, but is more depleted, probably due to cumulative effects.

418

419 **6. Radiogenic (Sr and Nd) isotope analyses**

420 Representative samples from all extrusive sequences presented above have been analyzed
421 for Sr-Nd isotopes. Results are presented on Fig. 8.

422 All samples are relatively clustered in ϵNd_i with positive values between 6.68 and 9.21.
423 $^{87}\text{Sr}/^{86}\text{Sr}(t)$ is relatively more dispersed with values between 0.7045 and 0.7063. All rocks
424 plot out of the mantle correlation line (Fig. 8). There is a progression from high $^{87}\text{Sr}/^{86}\text{Sr}(t)$
425 values (around 0.7063) for the core of the seamount to lower values in the felsic rocks
426 (around 0.7055-0.706), and even lower values for the rejuvenation event in A and in the
427 mafic rocks of the B unit (between 0.7045 and 0.7055). Isotopic data on the Siah Kuh lavas
428 are comparable with data from other regional ophiolites (Fig.8; Oman: Godard et al., 2006;
429 Neyriz: Moghadam et al., 2014; Nain-Baft: Moghadam et al., 2013c).

430

431 **7. Mineral chemistry**

432 Bulk-rock analyses might be affected by hydrothermal alteration on the seafloor.
433 Consequently, compositions of unaltered clinopyroxenes and spinels in the rocks were
434 measured as they may yield direct information on the magmatic source. Compositional plots
435 for clinopyroxene are shown on Fig. 9a,b,c (after Leterrier et al., 1982) and for spinel on Fig.
436 9d (after Dick and Bullen, 1984). Detailed analyses of clinopyroxene and spinel are available
437 in the Supplementary Materials S1 and S2.

438

439 **Core of the seamount (A₁)**

440 Clinopyroxenes have low Ca+Na between 0.75-0.9 atoms per formula unit (apfu), low Ti
441 content (< 0.015 apfu) which place them in the tholeiitic to calc-alkaline basalt field of figure
442 9a, usually low Ti+Cr (average at 0.01 apfu) and high Ca (0.7-0.9 apfu) placing them in the

443 orogenic basalt field of figure 9b. Due to their low Ti content, they plot in the island arc
444 tholeiite field of figure 9c.

445

446 **Early rejuvenation in A**

447 Clinopyroxenes have higher Ti concentration of 0.02-0.04 apfu and low Ca+Na around 0.5-
448 0.8 apfu, high Ti+Cr (0.02-0.035 apfu), which place them in the mid-ocean ridge tholeiite
449 field of figures 9a and 9b.

450

451 **Late rejuvenation in A**

452 Clinopyroxenes have low Ca+Na concentration of 0.7-0.9 apfu, placing them in the
453 subalkaline field, and high Ti+Cr of 0.02-0.05 apfu placing them in the mid-ocean ridge
454 tholeiite field of figures 9a and 9b.

455

456 **B unit gabbro**

457 Clinopyroxenes from sample 1532 have Ca+Na concentrations between 0.85 and 0.92 apfu,
458 placing them mostly in the subalkaline field (Fig. 9a), and high Ti+Cr of 0.03-0.035 apfu
459 placing them in the mid-ocean ridge tholeiite field in figure 9b.

460

461 **B unit diabase**

462 Clinopyroxenes have low Ca+Na concentration between 0.7-0.8 apfu, placing them in the
463 subalkaline field (Fig. 9a), and high Ti+Cr of 0.02-0.045 apfu placing them in the mid-ocean
464 ridge tholeiite field in figure 9b.

465

466 **B unit basalt**

467 Clinopyroxene has 0.75-0.85 apfu Ca+Na, placing them in the subalkaline field (Fig. 9a), and
468 high Ti+Cr of 0.02-0.04 apfu placing them in the mid-ocean ridge tholeiite field (Fig. 9b).

469

470 **Spinel in ultramafic rocks**

471 Two generations of spinels have been analyzed in an ultramafic rock from A, with similar
472 lobate (magmatic) textures yet no textural relationships (Fig. 9d, Supplementary Material
473 S5). One has Cr# of 0.44-0.54, Mg# of 0.60-0.66 and Ti < 0.0018 apfu, while the other has
474 higher Cr# of 0.69-0.75, Mg# of 0.50-0.55 and Ti of 0.0010-0.0032 apfu. The first generation

475 plots in the overlap between the abyssal and supra-subduction fields, while the second
476 generation has clear supra-subduction signatures (Fig. 9d). Spinels in ultramafics from B have
477 a wide range of Ti concentrations (0.002-0.025 apfu), a likely indicator of a cumulative origin.
478 The Ti content increases toward the top of the ultramafic sequence. The lowermost spinels
479 compare with the first generation of the A unit, with similar Cr# (0.46-0.52) but slightly lower
480 Mg# (0.66-0.7).

481

482 **8. Zircon U-Pb dating and Hf isotope analyses**

483 Zircons have been separated from four different kinds of rocks, belonging to the A unit
484 (#1518, rhyolite) and the B unit (#1720, anorthosite; 1532, gabbro; 1432, basalt). Zircons are
485 abundant in anorthosite and gabbro, but scarce in rhyolite and basalt. Most of them have
486 clear magmatic textures (Supplementary Material S3). Only concordant zircons were
487 considered. Zircon cathodoluminescence images, trace element analyses and trace element
488 diagrams are available in the Supplementary Materials S3, S4 and S5 respectively.

489

490 **Rhyolite in A**

491 Despite the small number of zircons in the rock, five concordant zircons show strong
492 inheritance with ages scattered between 1800 and 87 Ma (Fig. 10a). The youngest zircon
493 population (n=2) defines a maximum age with a weighted average of 87.0 ± 1.8 Ma. These
494 two zircons have positive ϵ_{Hf} around 10, and T_{DM} ages around 500 Ma (Fig. 11).

495

496 **Gabbro in B**

497 Thirteen concordant zircons yield a weighted average age of 77.8 ± 0.98 Ma (Fig. 10b). Single
498 ^{238}U - ^{206}Pb ages are scattered between 81 and 75 Ma. All the zircons have very positive ϵ_{Hf}
499 values around 14 and T_{DM} ages around 270 Ma (Fig. 11).

500

501 **Anorthosite in B**

502 Fourteen concordant zircons yield a weighted average age of 77.3 ± 1.5 Ma (Fig. 10c). Single
503 ^{238}U - ^{206}Pb ages are scattered between and 82 and 73 Ma. Most of these zircons have
504 positive ϵ_{Hf} values around 9 and T_{DM} ages around 540 Ma (Fig. 11).

505

506 **B unit basalt**

507 Despite the small number of zircons in the rock, five concordant zircons show strong
508 inheritance with ages scattered between 500 and 73 Ma (Fig. 10d). The youngest zircon
509 population (n=2) defines a maximum age for this basalt with a weighted average of $73.7 \pm$
510 1.3 Ma, with very distinct ϵ_{Hf} values of -3 and 16 (Fig. 11).

511

512 **9. Discussion**

513 **9.1. *Effects of seafloor alteration and metamorphism***

514 Seafloor alteration and metamorphism can modify significantly the chemical composition of
515 ophiolitic rocks. Major elements can vary a lot through intense hydration of rocks
516 (represented by LOI, from 0.9 to 8.6 wt.%). Here, most of the hydration occurs at the
517 seafloor, as attested by the appearance of chlorite, epidote and pumpellyite (e.g. Fig 4d,f).
518 Examining correlations between the amount of volatiles in the rock (LOI) and major and
519 trace-elements concentrations (Humphris and Thompson, 1978) can help decipher alteration
520 effects in the rock. In the studied samples Si and Na are inversely correlated with the LOI,
521 even when not considering felsic rocks that are usually much less hydrated than basalts
522 (Supplementary Materials S6). Bulk rock major elements such as Si, Na, K, Ca and trace
523 elements including Cs, Rb, Ba, Sr (LILE) are modified by seafloor alteration (Frey and Weis,
524 1995; Gillis, 1995), questioning the relevance of the TAS and AFM diagrams for altered
525 oceanic rocks. Relict clinopyroxenes are likely trustworthy indicators of the chemistry of the
526 magma, as they are primary minerals with a composition that is governed at first order by
527 the partition coefficients of elements with the magma (Leterrier et al., 1982). Destabilization
528 or recrystallization of clinopyroxene is harder than that of plagioclase (e.g. Spilde et al.,
529 1993).

530 Instead, most high field strength elements (HFSEs), and rare earth elements (REEs) are
531 generally considered to be immobile during alteration (e.g. Cann, 1970). Rock classification
532 based on immobile elements should however be used with care, and cannot replace a
533 careful petrographic examination, as rhyolites in our study were misclassified as andesites in
534 the Zr/Ti – Nb/Y. Trace element ratios used in discrimination diagrams as well Sr, $^{87}\text{Sr}/^{86}\text{Sr}(t)$,
535 Nd and ϵ_{Nd_i} values show no correlation with LOI (Suppl. Material S11). Seawater alteration is
536 however commonly cited as one of the main factors affecting $^{87}\text{Sr}/^{86}\text{Sr}$ signatures of altered
537 lavas (Hauff et al., 2003; Kawahata et al., 2001). A careful examination of the Sr isotopic
538 signatures shows a negative correlation between the Sr or REE and $^{87}\text{Sr}/^{86}\text{Sr}$ (Suppl. Material

539 S12), trending toward seawater compositions This is best explained by a relatively stronger
540 effect of seawater alteration on rocks that initially contain little Sr, i.e. the most depleted
541 rocks.

542 Incipient blueschist metamorphism of the whole Siah Kuh unit (at ~200-250°C, 0.6-0.9 GPa)
543 should also be considered as it is associated with fluid circulation (Bonnet et al., 2019a).
544 However, rocks never fully equilibrate at these conditions making the metamorphic imprint
545 very limited (and restricted to some magmatic rocks of the B unit). Associated fluid
546 circulations at T<300°C make alteration during metamorphism less likely than alteration at
547 the seafloor. Further we only discuss the petrogenesis based on alleged immobile elements.

548

549 ***9.2. Evolution of geochemical signatures and tectonomagmatic setting***

550 The Siah Kuh seamount is the ideal place to study the evolution of the magmatic source of
551 an ophiolite: unlike most ophiolitic “mélanges” or large-scale ophiolites (save the Oman
552 ophiolite), the structural framework as well as relative and absolute magmatic chronologies
553 are well-constrained here. Furthermore, the Siah Kuh seamount records the evolution of
554 lava chemistry in a single area, so that variations through time may reflect either mantle
555 heterogeneities, viscous flow and/or chemical changes of the composition through time (i.e.,
556 due to melt extraction, fluid circulation or source mixing).

557

558 **An initial supra-subduction event**

559 The supra-subduction origin of altered magmatic rocks may be reflected by four mostly
560 independent trends in the trace elements: (1) rare-earth elements-depleted melts (due to
561 the melting of an already depleted mantle, König et al., 2010), (2) HFSE (including Ti, Nb, Ta,
562 Zr, Hf) depletion compared to REE elements (due to trapping by refractory phases such as
563 Fe-Ti oxides; Briquieu et al., 1984; Gao et al., 2007), (3) V enrichment due to oxidizing
564 conditions above subduction zones enhancing the solubility of V (Shervais, 1982), and (4)
565 enrichment of the source in LREE and Th by sediment-derived fluids (including melts, König
566 et al., 2010; Plank, 2005). The contamination of the source by sediment-derived melts also
567 leads to a strong decrease of ϵNd toward sedimentary values (around -8, Plank and
568 Langmuir, 1998; e.g. Kusano et al., 2017). These trends are variably observed in the rocks
569 from the A₁ unit (core of the seamount) and in the felsic rocks of B.

570 The lowermost basalts in A₁ are slightly depleted in rare-earth elements (Fig. 6a), in HFSE
571 (Nb-Ta and small Ti negative anomalies, Fig. 6b and Fig 7a,b,c), but do not show enrichment
572 in Th or V (except for one sample, #1628, that is higher in the sequence; Fig. 7a,d). These
573 signatures are typical of arc tholeiites. Clinopyroxene compositions from the A₁ basalts also
574 show sub-alkaline signatures and are comparable to IAT clinopyroxenes (Fig. 9). Sr-Nd
575 isotopes have clustered values of εNd (6.93-7.57), yet variable Sr isotopic ratios (0.70551-
576 0.70633; Fig. 8). The high εNd values preclude any significant contribution from sediments
577 melts to the mantle source. High ⁸⁷Sr/⁸⁶Sr values are best explained by hydrothermal
578 alteration of the basalts (Suppl. Material S12), as is commonly expected for altered oceanic
579 rocks (e.g. Godard et al., 2006; Hauff et al., 2003; Kawahata et al., 2001).

580 Felsic rocks from A and B have uniform chemical compositions, with a strong depletion in
581 HFSE (Fig. 6d, 7a,c) and small enrichment in Th (Fig. 7a,d). εNd values (6.98-7.25) are
582 comparable to those of the basalts.

583 Boninites show a strong depletion in rare earth elements (Fig. 6a) and Ti (Fig. 7b), but
584 enrichment in Th and V (Fig. 7a,b). There are no Nd isotope measurements on these rocks.

585 There are no clues for high-pressure melting of slab lithologies (i.e. in the garnet stability
586 field, which would result in HREE-depleted adakitic magmas; e.g. Martin, 1999).

587 This set of data advocates for several partial melting events of a metasomatized supra-
588 subduction mantle source, with limited contamination by sediment-derived melts (at least
589 for the arc tholeiites and felsic rocks, likely involving more sediments in the boninites; Haase
590 et al., 2015; Ishikawa et al., 2005; Kusano et al., 2017). Hence the A₁ (core) unit of the Siah
591 Kuh seamount and the felsic rocks in the B unit represents the magmatic evolution of an
592 intraoceanic arc from an IAT to IAT/calc-alkaline-transitional felsic rocks and boninites. This
593 evolution is similar to what is currently recorded in intraoceanic arc systems, notably at the
594 initiation of subduction (e.g. Belgrano and Diamond, 2019; Hawkins et al., 1984; Pearce et
595 al., 1984; Stern and Bloomer, 1992).

596 Concordant zircons have been analyzed in a rhyolite from this event. They show a broad
597 range of ages (1823-85.7 Ma), but the youngest population (2 zircons) was dated at 87.0 ±
598 0.9 Ma, and is a plausible age for eruption, given the Campanian-Maastrichtian age of
599 overlying sediments proposed by Sabzehei (1974). The lowermost basalts (core of A unit
600 basaltic rocks) upon which this rhyolite was erupted should be somewhat older. Xenocrystic
601 zircons might originate from sediment melts possibly contaminating the mantle source

602 (although the contribution of sediment melts to the source of these rocks is very limited), or
603 they were more likely assimilated from the sub-arc crust during eruption.

604

605 **A MORB rejuvenation event**

606 In sharp contrast with the A₁ unit, lavas erupted above sediments (i.e. in the A₁'-A₂-A₃-A₄ and
607 B units) show no strong depletion in rare-earth elements (Fig. 6e), very limited-to-absent
608 HFSE negative anomalies (Fig. 6f) and no Th enrichment (Fig. 7a,d), i.e. no supra-subduction
609 signatures. They are in fact clustered in two trends (with some internal variability): the early
610 stage lavas show an E-MORB-like signature while the late stage is characteristic of N-MORB
611 (Fig. 6e,f and Fig. 7). A similar trend is observed in mafic rocks of the B unit (Fig. 6g,h), which
612 is thus likely to be a lateral equivalent of A, as suggested by the spatial association and the
613 correlation of lithologies. Clinopyroxene analyses confirm their mid-ocean ridge tholeiitic
614 signature (Fig. 9). The positive ϵNd of basalts (6.83 to 9.21; Fig. 8) is compatible with a
615 moderately depleted mantle source (Patchett, 1983). E-MORB and N-MORB lavas are
616 generated in modern oceans at mid-ocean ridges (Michael, 1995; Niu et al., 1999) and in
617 back-arc spreading centers (e.g. Stern et al., 1990). In the latter configuration, the
618 subduction signature is very variable, but its absence may be characteristic of a large
619 distance from the subduction and/or influence from a more primitive mantle (e.g. Lau Basin,
620 Volpe et al., 1988; Mariana back-arc, Pearce et al., 2005).

621 Anorthosite and gabbro in the B unit are two favorable lithologies for zircon dating. Both
622 rocks have similar ages within uncertainty around 77-78 Ma. The dated gabbro (#1532) has
623 REE and trace element profiles similar to N-MORB, and no obvious HFSE negative anomalies
624 (Fig. 6g,h). Its textural characteristics, reminiscent of cumulates (i.e. similar to some
625 observed on the Mid-Atlantic ridge, Tiezzi and Scott, 1980; depletion in REE and Eu positive
626 anomaly, Seifert et al., 1996), make it unsuitable for discrimination diagrams of figure 7.
627 Clinopyroxene analyses plot in the mid-ocean ridge tholeiite field (Fig. 9). This suggests that
628 this gabbro has a (likely N-) MORB affinity. An attempt to date zircons in basalts from top of
629 the B unit yielded a broad range of ages (1080-73.1 Ma), with a youngest population (two
630 zircons) giving a plausible eruption age of 73.7 ± 0.7 Ma that must be cautiously interpreted.
631 These Late Cretaceous ages are consistent with the relative chronology and the mapped
632 Upper Cretaceous sediments.

633 These data reveal a multistage magmatic history for the Siah Kuh seamount, which evolved
634 from arc tholeiite and boninite to calc-alkaline-transitional possibly until ~87 Ma, and later
635 experienced a distinct magmatic episode of E-to-N-MORB affinity, starting around 77.5 Ma
636 and possibly lasting until 73 Ma (Figs. 7a, 10).

637

638 **9.3. Constraints on the nature and evolution of the underlying mantle**

639 Mantle rocks found in the Siah Kuh unit are mainly serpentinized dunites (A unit) and
640 cumulates (B unit). The high Cr# of spinels are characteristic of a depleted mantle (Dick and
641 Bullen, 1984; Moll et al., 2007). However, a second generation of Cr-richer spinel in a dunite
642 of the A unit might have formed by impregnation of the mantle by boninitic melts during
643 island arc volcanism (e.g. Barnes and Roeder, 2001).

644 The restricted spread of the ϵNd_i values accross all magmatic rocks analyzed suggest the
645 melting of a mantle source without a significant contribution from sediment melts (<1%), in
646 particular during the arc stage, when it is most expected (e.g. Zamboni et al., 2016). This
647 signature might however exist in boninites (not analyzed for Nd isotopes) that show a
648 significant Th enrichment. Hence, ϵNd_i values around 6-10 likely reflect the composition of a
649 slightly heterogeneous mantle that was not strongly contaminated by sediments during the
650 subduction responsible for arc formation. These values are very similar to those of other
651 regional ophiolites (Oman, Godard et al., 2006; Neyriz, Moghadam et al., 2014b; Nain-Baft,
652 Moghadam et al., 2013c), and are comparable with the abnormal modern Indian Ocean
653 MORB (likely refertilized by old subductions; Dupré and Allègre, 1983; Xu and Castillo, 2004).
654 $\epsilon\text{Hf}(t)$ values of zircons are in majority positive (2 values are negative), around 14 for gabbro
655 and 9 for plagiogranite, which points to partially-depleted mantle sources with some
656 heterogeneity.

657 The evolution from supra-subduction to MORB signatures is opposite to what is observed in
658 many other ophiolites (e.g. Oman, Godard et al., 2003, Albania, Dilek et al., 2008), commonly
659 explained by progressive contamination of the mantle by subduction-derived fluids and
660 melts (occurring in ~1 My, Rioux et al., 2013). Instead, our observations are reminiscent of
661 longer-term processes (~10 My) occurring in modern arc-back-arc systems, such as the
662 Marianas: while the arc itself has a strong supra-subduction signature, back-arc lavas only
663 show a limited subduction component, due to the upwelling of uncontaminated mantle
664 (Pearce et al., 2005). The dissipation of the subduction signature could also be explained by

665 the end of subduction and the replacement of the underlying mantle facilitated by fast
666 horizontal asthenospheric flow (e.g. Faccenna et al., 2014).

667 The transition from E-MORB to N-MORB lavas (Fig 10) during the rejuvenation event might
668 be linked with (1) initial heterogeneity of the mantle, (2) a progressive depletion of an
669 initially enriched mantle source due to melt extraction, or (3) changes in the fusion rate of a
670 depleted mantle source. E-MORB lavas are usually thought to stem from plume enrichment
671 of the mantle or assimilation of formerly erupted lavas (e.g. Hémond et al., 2006). The
672 generation of N-MORB lavas could then result from a progressive depletion of this mantle
673 wedge due to melt extraction. An alternative way to form N-MORB lavas after E-MORB
674 basalts from the same depleted mantle source would merely require an increase of the
675 fusion rate by a few percents. However, this process would not explain the variability of the
676 Nb/Yb and Th/Yb ratios as well as the variability of zircon $\epsilon\text{Hf}(t)$ values and whole rock ϵNd
677 values, that require some heterogeneity in the underlying mantle. The Late Permian T_{DM} age
678 of zircons in gabbro might relate to the fusion of a mantle depleted during the Late Permian,
679 which corresponds to widespread magmatism on both sides of the Neotethys (potentially
680 plume-related, Ghasemi et al., 2002; Lapierre, 2004). Older (~ 550 Ma) T_{DM} in the anorthosite
681 could however relate to crustal contamination.

682 Finally, the presence of old zircons xenocrysts (200 Ma to 1.7 Ga) in Siah Kuh magmatic
683 rocks as well as granitoid xenoliths in the Siah Kuh volcanics (2-3-cm-long angular granitic-
684 to-granodioritic enclaves according to Sabzehei (1974) – though never observed in our
685 study) might reflect the nature of the sub-arc crust, partially assimilated during the ascent of
686 magma, or subducted sediments in the source (although this hypothesis is less likely given
687 the very limited contribution of sediments to the source). The ages of these zircons indeed
688 correspond to magmatic events recorded in the continental margins of the Neotethys
689 (Ahmadipour et al., 2003; Ghasemi et al., 2002; Moghadam et al., 2017).

690

691 **9.4. Geodynamic reconstructions of the Neotethys realm**

692 9.4.1. Chronological overview

693 The regional record of processes described below is detailed in Table 2.

694 **Initial rifting and early spreading history (Permian to Jurassic)**

695 In the Siah Kuh region, the magmatic history associated with rifting and early spreading of
696 the Neotethys is relatively well preserved in the Sikhoran complex: Late Permian to Late

697 Triassic gabbroic complexes have enriched to depleted tholeiitic signatures, with some
698 crustal contamination (Ahmadipour et al., 2003), and partially intrude the overlying
699 metamorphics. The end of high temperature metamorphism and anatexis of Sargaz-Abshur
700 sediments around 200 Ma (Early Jurassic; Ghasemi et al., 2002) are coeval with the sealing of
701 both igneous and metamorphic rocks by Lower Jurassic unmetamorphosed sediments
702 (Sabzehei, 1974). The Sikhoran complex would thus correspond to a Jurassic Ocean-
703 Continent Transition (e.g. Péron-Pinvidic and Manatschal, 2009) on the Northern Side of the
704 Neotethys. Equivalents would be the Bajgan-Durkan complex and the ultramafic Sorkhband-
705 Rudan massif (Delavari et al., 2016; Hunziker et al., 2015; McCall, 1997). Some of the rifting
706 history is recorded throughout Zagros and in Oman by the association of the Upper Triassic
707 to “Mid”-Cretaceous deep sediments (grabens) and shallow sediments, the latter being
708 described as allochthons or “Exotics” (Gharib and De Wever, 2010; Jannessary and
709 Whitechurch, 2008; Ricou, 1974; Ricou et al., 1977; Searle and Graham, 1982; Wrobel-
710 Daveau et al., 2010). Triassic to Liassic alkaline lavas (Ricou, 1974; Sacconi et al., 2013;
711 Searle, 1980; Whitechurch et al., 2013) are precursors to Liassic volcanic sequences with E-
712 MORB affinities (although rarely exposed, e.g. Moghadam et al., 2017, 2013b; Searle, 1980).

713

714 **Subduction: arc development at the northern margin (Jurassic-Oligocene) and Cretaceous-** 715 **Paleocene back-arcs**

716 The structure of the Zagros suture zone suggests a strong inheritance from northward
717 subduction of the Neotethys/Arabian Plate below Iran (e.g. Agard et al., 2011), yet the
718 timing of subduction initiation is not well-constrained. Abundant subduction-related
719 magmatism has been associated with this subduction (Berberian and Berberian, 1981;
720 Omrani et al., 2008 and references therein). Although Early to Mid-Jurassic calc-alkaline
721 magmatism (e.g. Jafari et al., 2018; Shahbazi et al., 2010) suggests subduction initiation
722 during the Early Jurassic (see also the compilation of Hassanzadeh and Wernicke, 2016; their
723 figure 7), this interpretation is challenged by some authors, who outline that subduction
724 signatures could be related to crustal contamination (Azizi and Stern, 2019; Barbarin, 1999;
725 Hunziker et al., 2015). Instead, these authors propose an inception of subduction during Late
726 Cretaceous, which is however inconsistent with the recovery of ‘mid’ Cretaceous blueschists
727 made of Neotethyan seafloor in Zagros and Makran (as early as 120 Ma in Zagros, Agard et
728 al., 2006; Moghadam et al., 2017; and 100 Ma in Makran, Delaloye and Desmons, 1980), and

729 with Zagros eclogites possibly formed during Neotethyan subduction (with ages ~185-170
730 Ma, Davoudian et al., 2008, 2016).

731 Extension and spreading interpreted as back-arc in the Eurasian upper plate (Nain-Baft,
732 Sistan and Sabzevar basins), which started during Albian/Aptian (~125-100 Ma; Babazadeh
733 and de Wever, 2004; Moghadam et al., 2014a, 2009; Rossetti et al., 2010; Zarrinkoub et al.,
734 2012), also require that subduction started at least during Early Cretaceous.

735 Arc magmatism was recorded continuously in Southern Iran, in the Sanandaj-Sirjan zone
736 (until the Late Cretaceous; Jafari et al., 2018), the Kermanshah arc (Paleocene-Eocene;
737 Whitechurch et al., 2013), and the Urumieh-Dokhtar magmatic arc (post-Eocene; Omrani et
738 al., 2008).

739

740 **Late Cretaceous compressional event**

741 A main feature of the Neotethys is the intra-oceanic subduction that started at the end of
742 the Early Cretaceous in various areas (e.g. Oman, Neyriz, Turkey; Table 2), leading to the
743 emplacement of supra-subduction ophiolites and metamorphic soles (e.g. Hacker et al.,
744 1996).

745 Rocks from the core of the Siah Kuh seamount are very similar to those from the V2 stage in
746 the Semail ophiolite, in particular arc tholeiites and boninites (Alabaster et al., 1982;
747 Belgrano and Diamond, 2019; Godard et al., 2003; Ishikawa et al., 2005). This V2 event,
748 dated between 96.4 and 95.5 Ma (Rioux et al., 2013, 2012) is older than what is dated in Siah
749 Kuh. However, felsic intrusives in the Semail ophiolite have been dated between 90 and 85
750 Ma (Gnos and Peters, 1993; Lippard et al., 1986; Searle, 1980) and could correspond to the
751 felsic rocks in Siah Kuh. The few My delay between forearc magmatism (arc tholeiites and
752 boninites) in Oman and intra-oceanic arc magmatism (felsic rocks) recorded in Oman (and
753 potentially in the Siah Kuh unit) corresponds to the time required for the transition between
754 forearc and arc signatures (7-8 Myr in the Bonin arc; Ishizuka et al., 2011). The Neyriz and
755 Kermanshah ophiolitic complexes in Zagros potentially record similar processes (Babaie et
756 al., 2006, 2001; Delaloye and Desmons, 1980; Jannessary, 2003; Lanphere and Pamić, 1983;
757 Monsef et al., 2018a; Whitechurch et al., 2013).

758 Subduction initiation was linked with a compressive event (Agard et al., 2007, 2014)
759 responsible for the exhumation of blueschists all along the Neotethys from Turkey to the

760 Western Himalayas (Monié and Agard, 2009), as well as initiation of subduction within back-
761 arcs (e.g. Sabzevar: Rossetti et al., 2010; Sistan: Bonnet et al., 2018).

762 While arc magmatism is only subordinate in Oman, the Siah Kuh seamount core (A₁ unit),
763 formed around 87 Ma, may represent the arc products of this southern, intra-oceanic
764 subduction (see further discussion below).

765

766 **Evidence for a second Late Cretaceous spreading phase**

767 This study reports a Late Cretaceous MORB-type magmatic event in the Neotethys (i.e., B
768 unit and magmatic rejuvenation in A unit). In the Kermanshah ophiolite, a magmatic event at
769 ~79 Ma (Ao et al., 2016) was likely associated with a slow-spreading event (Wrobel-Daveau
770 et al., 2010). E-MORB dykes dated at ~81 and ~76 Ma in the Sikhoran complex (Ahmadipour
771 et al., 2003; Ghasemi et al., 2002) could also correspond to this magmatic event. In
772 comparison, an arc-related magmatic phase is recorded during the Late Cretaceous in the
773 Nain-Baft-North Makran ophiolites (Kananian et al., 2001; Monsef et al., 2018b).

774 The magmatic evolution observed in the Siah Kuh seamount hints to the change from an arc
775 to back-arc-like setting, and its possible original location in the Neotethys is therefore
776 discussed below.

777

778 9.4.2. Where was the arc?

779

780 The Siah Kuh seamount is presently sandwiched within the Zagros suture zone and domed
781 below other exposures of Zagros blueschists and of the Sikhoran complex (e.g. Agard et al.,
782 2006; Angiboust et al., 2016). Although challenged by some authors (e.g. Moghadam and
783 Stern, 2015), there is generally a consensus on the existence of two north-dipping
784 subduction zones within the Neotethys (e.g. Coleman, 1981; Searle and Cox, 1999; Rossetti
785 et al., 2010; Agard et al., 2011): (1) the long-lived North-Neotethys subduction zone initiated
786 during the Jurassic and lasting until Eocene, and (2) the short-lived South Neotethys
787 subduction zone initiated in mid-Cretaceous times and terminated by the Late Cretaceous
788 with the continental subduction of the Arabian platform (Agard et al., 2010; Searle et al.,
789 2004).

790 Geochemical evidence suggest that Siah Kuh formed in an intraoceanic forearc/arc setting,
791 and later evolved in a back-arc setting. Whether this occurred in the upper plate of

792 subduction (1) or (2) is unclear. We hereafter discuss two different scenarii featured in figure
793 12b and 12c.

794

795 **Hypothesis 1: Arc of the Southern Intra-Neotethys Subduction**

796 Most of the magmatic activity documented in the Southern Neotethys (e.g. Neyriz, Oman)
797 occurred around 95 Ma (e.g. Monsef et al., 2018a; Rioux et al., 2012; see Table 2). The 87
798 Ma age recorded within Siah Kuh is approximately 10 Ma younger than supra-subduction
799 magmatism. At this time, the Semail ophiolite underwent a $\sim 140\text{-}150^\circ$ clockwise rotation
800 and recorded alkaline magmatism (Morris et al., 2016; Umino, 2012; van Hinsbergen et al.,
801 2019). However, subduction had not ended yet (as shown by later subduction and blueschist
802 to eclogite metamorphism of the Arabian margin; e.g. El Shazly et al., 2001; Searle et al.,
803 2004; Yamato et al., 2007) and partial melting may have occurred in the mantle north of the
804 Semail ophiolite (Fig. 12b). Resulting magmas would probably be erupted on early Mesozoic
805 oceanic crust, possibly in the presence of extensional allochtons similar to those of the
806 Sargaz-Abshur complex. The development of an arc system more mature than in Oman (i.e.,
807 including true calc-alkaline magmas) could be favored by deeper and stronger hydration of
808 the mantle wedge.

809 The ~ 78 Ma event recorded in Siah Kuh corresponds to the time when continental rocks
810 start to be exhumed (El Shazly et al., 2001; Yamato et al., 2007). Resistance to the
811 convergence and subduction of the Arabian platform, combined with the slab pull generated
812 by the deeper oceanic slab could induce slab roll back, possibly followed by slab break off (a
813 deep slab was imaged by van der Meer et al., 2018). This process, modeled by Chemenda et
814 al. (1996), may have generated back-arc extension in the upper plate. An asthenospheric
815 window would also allow the influx of heat as well as enriched mantle that could form the
816 MORB lavas. If the Siah Kuh unit was located in an arc/back-arc of the Southern Neotethys
817 Subduction, it would belong to the lower plate of the Northern Neotethys Subduction and
818 get subducted lately (i.e. close to collision, for example during the late Paleocene-Eocene)
819 along with remnants of the Early Mesozoic seafloor. This hypothesis easily explains its
820 underplating beneath the Ashin and Seghin blueschist facies units (Fig. 12b; Agard et al.,
821 2006a; Angiboust et al., 2016a).

822

823 **Hypothesis 2: Arc of the Northern Neotethys Subduction?**

824 The present position of the Siah Kuh unit below the other Zagros blueschists (Agard et al.,
825 2006) and sequential accretion outlined by Angiboust et al. (2016) make it difficult to
826 reconcile with a Northern Neotethys subduction zone (see Fig. 12b,c). The main argument
827 for a genesis in this context is a possible genetic link between the Sikhoran-Sargaz-Abshur
828 complexes and the Siah Kuh seamount, as discussed above. No clear arc magmatism at 87
829 Ma is however described in the obducted ophiolites (Semail-Neyriz) or in the Sanandaj-Sirjan
830 zone surrounding the Siah Kuh unit. Genesis of Siah Kuh above the Northern Neotethys
831 subduction would require the existence of extensional allochthons similar to the Sargaz-
832 Abshur complex (to explain the zircon distribution). Formation above the Northern
833 Neotethys subduction could explain the Late Cretaceous E-MORB dykes within the Sikhoran
834 complex. Arc magmatism in Siah Kuh likely corresponds to a magmatic event recorded in
835 Makran by detrital zircons aged 90-85 Ma, interpreted by Mohammadi et al. (2017) and Burg
836 (2018) to result from arc magmatism on the Northern margin of the Neotethys. However,
837 detrital zircons aged 80-75 Ma are not particularly abundant in these studies.

838 In this configuration, subduction of the Siah Kuh seamount would require (1) initiation of a
839 new subduction zone to the north of the Northern Tethys Subduction or (2) a northward
840 migration of the subduction zone, for example through a splay fault (dotted line in Fig. 12c).
841 Initiation of a new subduction zone above a pre-existing one is observed in Southeastern
842 Taiwan, where a large portion of the forearc gets subducted (e.g. Malavieille et al., 2002).
843 Boutelier et al. (2003) suggested that subduction initiation would occur preferentially in the
844 back-arc. In this configuration, however, subduction of the largely intact Siah Kuh seamount
845 would require a huge mega-splay fault, much larger than the one observed in the Nankai
846 accretionary wedge (Park et al., 2002).

847

848 **10. Conclusion**

849 The Siah Kuh unit is a former seamount, now outcropping in the Zagros Suture Zone. It is
850 composed of two units separated by a major thrust, both of which record a comparable
851 magmatic and geodynamic history:

- 852 1) The seamount was built around 87 Ma in an intraoceanic forearc/arc setting and
853 witnesses increasing maturity and metasomatism of the mantle wedge through time.
- 854 2) A resumption of magmatism occurred around 78-73 Ma in a back-arc-like setting,
855 with a transition from enriched to depleted lavas.

856 3) The Siah Kuh seamount was later subducted below the Eurasian plate (meanwhile,
857 the B unit was thrust onto the A unit), at ~30 km depth, and thereafter exhumed (Fig.
858 12a).

859 Combining structural and geochemical data from other magmatic and metamorphic
860 episodes in the Iranian-Omanese Neotethys realm (Table 2), which was affected by two
861 subduction zones during the Late Cretaceous, we propose two possible tectono-magmatic
862 settings for the Siah Kuh seamount. This exceptional remnant might represent (1) an arc
863 located above the Southern Neotethys subduction zone (Fig. 12b), and would therefore
864 represent a non-obducted piece (and the 'missing arc') of the Oman ophiolite, or (2) an arc
865 to forearc domain at the Northern Margin of the Neotethys (Fig. 12c). We consider the first
866 hypothesis more likely (Fig. 12b).

867
868

869 **Acknowledgements:**

870 This study was partly funded by the project “Zooming in between plates” (Marie Curie
871 International Training Network no. 604713) to Philippe Agard. We thank M. Fialin and N.
872 Rividi (CAMPARIS) for analytical support, E. Delairis (ISTeP) for the preparation of thin
873 sections, and Hong T. (IGGCAS) and Tan Z. (ISTeP) for help with zircon U-Pb-εHf data
874 collection and processing. M. Rioux, T. John, M. Soret and M. Locatelli are thanked for
875 insightful discussions.

876

877 **References:**

- 878 Agard, P., Jolivet, L., Vrielynck, B., Burov, E., Monié, P., 2007. Plate acceleration: The
879 obduction trigger? *Earth and Planetary Science Letters* 258, 428–441.
880 <https://doi.org/10.1016/j.epsl.2007.04.002>
- 881 Agard, P., Monié, P., Gerber, W., Omrani, J., Molinaro, M., Meyer, B., Labrousse, L.,
882 Vrielynck, B., Jolivet, L., Yamato, P., 2006. Transient, synobduction exhumation of Zagros
883 blueschists inferred from P-T, deformation, time, and kinematic constraints: Implications for
884 Neotethyan wedge dynamics. *Journal of Geophysical Research* 111, B11401.
885 <https://doi.org/10.1029/2005JB004103>
- 886 Agard, P., Omrani, J., Jolivet, L., Whitechurch, H., Vrielynck, B., Spakman, W., Monié, P.,
887 Meyer, B., Wortel, M.J.R., 2011. Zagros orogeny: a subduction-dominated process.
888 *Geological Magazine* 148, 692–725. <https://doi.org/10.1017/S001675681100046X>
- 889 Agard, P., Searle, M.P., Alsop, G.I., Dubacq, B., 2010. Crustal stacking and expulsion
890 tectonics during continental subduction: P-T deformation constraints from Oman. *Tectonics*
891 29. <https://doi.org/10.1029/2010TC002669>
- 892 Agard, P., Zuo, X., Funicello, F., Bellahsen, N., Faccenna, C., Savva, D., 2014. Obduction:
893 Why, how and where. Clues from analog models. *Earth and Planetary Science Letters* 393,

894 132–145. <https://doi.org/10.1016/j.epsl.2014.02.021>

895 Ahmadipour, H., Sabzehei, M., Whitechurch, H., Rastad, E., Emami, M.H., 2003. Soghan
896 complex as an evidence for paleospreading center and mantle diapirism in Sanandaj-Sirjan
897 Zone (South-East Iran). *Journal of Sciences, Islamic Republic of Iran* 14, 157–172.

898 Alabaster, T., Pearce, J.A., Malpas, J., 1982. The volcanic stratigraphy and petrogenesis of the
899 Oman ophiolite complex. *Contributions to Mineralogy and Petrology* 81, 168–183.
900 <https://doi.org/10.1007/BF00371294>

901 Ali, S.A., Buckman, S., Aswad, K.J., Jones, B.G., Ismail, S.A., Nutman, A.P., 2012.
902 Recognition of Late Cretaceous Hasanbag ophiolite-arc rocks in the Kurdistan Region of the
903 Iraqi Zagros suture zone: A missing link in the paleogeography of the closing Neotethys
904 Ocean. *Lithosphere* 4, 395–410. <https://doi.org/10.1130/L207.1>

905 Andersen, T., 2002. Correction of common lead in U-Pb analyses that do not report ²⁰⁴Pb.
906 *Chemical Geology* 192, 59–79. [https://doi.org/10.1016/S0009-2541\(02\)00195-X](https://doi.org/10.1016/S0009-2541(02)00195-X)

907 Angiboust, S., Agard, P., Glodny, J., Omrani, J., Oncken, O., 2016. Zagros blueschists:
908 Episodic underplating and long-lived cooling of a subduction zone. *Earth and Planetary
909 Science Letters* 443, 48–58. <https://doi.org/10.1016/j.epsl.2016.03.017>

910 Ao, S., Xiao, W., Khalatbari Jafari, M., Talebian, M., Chen, L., Wan, B., Ji, W., Zhang, Z.,
911 2016. U–Pb zircon ages, field geology and geochemistry of the Kermanshah ophiolite (Iran):
912 From continental rifting at 79 Ma to oceanic core complex at ca. 36 Ma in the southern Neo-
913 Tethys. *Gondwana Research* 31, 305–318. <https://doi.org/10.1016/j.gr.2015.01.014>

914 Arvin, M., Pan, Y., Dargahi, S., Malekizadeh, A., Babaei, A., 2007. Petrochemistry of the
915 Siah-Kuh granitoid stock southwest of Kerman, Iran: Implications for initiation of Neotethys
916 subduction. *Journal of Asian Earth Sciences* 30, 474–489.
917 <https://doi.org/10.1016/j.jseaes.2007.01.001>

918 Arvin, M., Robinson, P.T., 1994. The petrogenesis and tectonic setting of lavas from the Baft
919 Ophiolitic Mélange, southwest of Kerman, Iran. *Canadian Journal of Earth Sciences* 31, 824–
920 834. <https://doi.org/10.1139/e94-076>

921 Azizan, H., Naderi, N., Navazi, M., Poshtkuhi, M., Rashid, H., Abazari, Z., Haddadan, M.,
922 2007. Geological Map of Iran, 1 : 100000 series - Dolatabad.

923 Azizi, H., Stern, R.J., 2019. Jurassic igneous rocks of the central Sanandaj–Sirjan zone (Iran)
924 mark a propagating continental rift, not a magmatic arc. *Terra Nova*.
925 <https://doi.org/10.1111/ter.12404>

926 Babaie, H.A., Babaei, A., Ghazi, A.M., Arvin, M., 2006. Geochemical, ⁴⁰Ar/ ³⁹Ar age, and
927 isotopic data for crustal rocks of the Neyriz ophiolite, Iran. *Canadian Journal of Earth
928 Sciences* 43, 57–70. <https://doi.org/10.1139/e05-111>

929 Babaie, H.A., Ghazi, A.M., Babaei, A., La Tour, T.E., Hassanipak, A.A., 2001. Geochemistry
930 of arc volcanic rocks of the Zagros Crush Zone, Neyriz, Iran. *Journal of Asian Earth Sciences*
931 19, 61–76. [https://doi.org/10.1016/S1367-9120\(00\)00012-2](https://doi.org/10.1016/S1367-9120(00)00012-2)

932 Babazadeh, S.A., de Wever, P., 2004. Early Cretaceous radiolarian assemblages from
933 radiolarites in the Sistan Suture (eastern Iran). *Geodiversitas* 26, 185–206.

934 Bagheri, S., Stampfli, G.M., 2008. The Anarak, Jandaq and Posht-e-Badam metamorphic
935 complexes in central Iran: New geological data, relationships and tectonic implications.
936 *Tectonophysics* 451, 123–155. <https://doi.org/10.1016/j.tecto.2007.11.047>

937 Barbarin, B., 1999. A review of the relationships between granitoid types, their origins and
938 their geodynamic environments. *Lithos* 46, 605–626. [https://doi.org/10.1016/S0024-4937\(98\)00085-1](https://doi.org/10.1016/S0024-4937(98)00085-1)

940 Barnes, S.J., Roeder, P.L., 2001. The Range of Spinel Compositions in Terrestrial Mafic and
941 Ultramafic Rocks. *Journal of Petrology* 42, 2279–2302.
942 <https://doi.org/10.1093/petrology/42.12.2279>

943 Barrier, E., Vrielynck, B., 2008. Palaeotectonic Maps of the Middle East: Late Maastrichtian.

944 Commission de la Carte Géologique du Monde Map 8.
945 Batiza, R., Vanko, D., 1984. Petrology of young Pacific Seamounts. *Journal of Geophysical*
946 *Research* 89, 11,211-235,260. <https://doi.org/10.1029/JB089iB13p11235>
947 Belgrano, T.M., Diamond, L.W., 2019. Subduction-zone contributions to axial volcanism in
948 the Oman–U.A.E. ophiolite. *Lithosphere* 11, 399–411. <https://doi.org/10.1130/L1045.1>
949 Berberian, F., Berberian, M., 1981. Tectono-plutonic episodes in Iran, in: Gupta, H.K.,
950 Delany, F.M. (Eds.), *Geodynamics Series*, Geodynamics Series. American Geophysical
951 Union, pp. 33–69.
952 Bonnet, G., Agard, P., Angiboust, S., Fournier, M., Omrani, J., 2019a. No large earthquakes
953 in fully exposed subducted seamount. *Geology* 47, 407–410.
954 <https://doi.org/doi.org/10.1130/G45564.1>
955 Bonnet, G., Agard, P., Angiboust, S., Monié, P., Fournier, M., Caron, B., Omrani, J., 2019b.
956 Structure and metamorphism of a subducted seamount (Zagros suture, Southern Iran).
957 *Geosphere* 15. <https://doi.org/10.1130/GES02134.1>.
958 Bonnet, G., Agard, P., Angiboust, S., Monié, P., Jentzer, M., Omrani, J., Whitechurch, H.,
959 Fournier, M., 2018. Tectonic slicing and mixing processes along the subduction interface: The
960 Sistan example (Eastern Iran). *Lithos* 310–311, 269–287.
961 <https://doi.org/10.1016/j.lithos.2018.04.016>
962 Boudier, F., Ceuleneer, G., Nicolas, A., 1988. Shear zones, thrusts and related magmatism in
963 the Oman ophiolite: Initiation of thrusting on an oceanic ridge. *Tectonophysics* 151, 275–296.
964 [https://doi.org/10.1016/0040-1951\(88\)90249-1](https://doi.org/10.1016/0040-1951(88)90249-1)
965 Boutelier, D., Chemenda, A., Burg, J.-P., 2003. Subduction versus accretion of intra-oceanic
966 volcanic arcs: insight from thermo-mechanical analogue experiments. *Earth and Planetary*
967 *Science Letters* 212, 31–45. [https://doi.org/10.1016/S0012-821X\(03\)00239-5](https://doi.org/10.1016/S0012-821X(03)00239-5)
968 Bouvier, A., Vervoort, J.D., Patchett, P.J., 2008. The Lu–Hf and Sm–Nd isotopic composition
969 of CHUR: Constraints from unequilibrated chondrites and implications for the bulk
970 composition of terrestrial planets. *Earth and Planetary Science Letters* 273, 48–57.
971 <https://doi.org/10.1016/j.epsl.2008.06.010>
972 Briquieu, L., Bougault, H., Joron, J.L., Gbochimie, I.L. De, Cg, G., Sciences, U.E.R., Terre,
973 D., Bataillon, U.S.T.L.P.E., Montpellier, C., 1984. Quantification of Nb, Ta, Ti and V
974 anomalies in magmas associated with subduction zones: petrogenetic implications. *Earth and*
975 *Planetary Science Letters* 68, 297–308.
976 Burg, J.-P., 2018. Geology of the onshore Makran accretionary wedge: Synthesis and tectonic
977 interpretation. *Earth-Science Reviews* 185, 1210–1231.
978 <https://doi.org/10.1016/j.earscirev.2018.09.011>
979 Cann, J.R., 1970. Rb, Sr, Y, Zr and Nb in some ocean floor basaltic rocks. *Earth and*
980 *Planetary Science Letters* 10, 7–11. [https://doi.org/10.1016/0012-821X\(70\)90058-0](https://doi.org/10.1016/0012-821X(70)90058-0)
981 Casey, J.F., Dewey, J.F., 1984. Initiation of subduction zones along transform and accreting
982 plate boundaries, triple-junction evolution, and forearc spreading centres—implications for
983 ophiolitic geology and obduction. *Geological Society, London, Special Publications* 13, 269–
984 290. <https://doi.org/10.1144/GSL.SP.1984.013.01.22>
985 Chemenda, A.I., Mattauer, M., Bokun, A.N., 1996. Continental subduction and a mechanism
986 for exhumation of high-pressure metamorphic rocks: new modelling and field data from
987 Oman. *Earth and Planetary Science Letters* 143, 173–182. [https://doi.org/10.1016/0012-](https://doi.org/10.1016/0012-821X(96)00123-9)
988 [821X\(96\)00123-9](https://doi.org/10.1016/0012-821X(96)00123-9)
989 Cloos, M., 1993. Lithospheric buoyancy and collisional orogenesis: subduction of oceanic
990 plateaus, continental margins, island arcs, spreading ridges, and seamounts. *Geological*
991 *Society of America Bulletin* 105, 715–737. [https://doi.org/10.1130/0016-](https://doi.org/10.1130/0016-7606(1993)105<0715:LBACOS>2.3.CO)
992 [7606\(1993\)105<0715:LBACOS>2.3.CO](https://doi.org/10.1130/0016-7606(1993)105<0715:LBACOS>2.3.CO)
993 Coleman, R.G., 1981. Tectonic setting for ophiolite obduction in Oman. *Journal of*

994 Geophysical Research 86, 2497–2508. <https://doi.org/10.1029/JB086iB04p02497>

995 Davoudian, A.R., Genser, J., Dachs, E., Shabanian, N., 2008. Petrology of eclogites from
996 north of Shahrekord, Sanandaj-Sirjan Zone, Iran. *Mineralogy and Petrology* 92, 393–413.
997 <https://doi.org/10.1007/s00710-007-0204-6>

998 Davoudian, A.R., Genser, J., Neubauer, F., Shabanian, N., 2016. $^{40}\text{Ar}/^{39}\text{Ar}$ mineral ages of
999 eclogites from North Shahrekord in the Sanandaj–Sirjan Zone, Iran: Implications for the
1000 tectonic evolution of Zagros orogen. *Gondwana Research* 37, 216–240.
1001 <https://doi.org/10.1016/j.gr.2016.05.013>

1002 Delaloye, M., Desmons, J., 1980. Ophiolites and melange terranes in Iran: A
1003 geochronological study and its paleotectonic implications. *Tectonophysics* 68, 83–111.
1004 [https://doi.org/10.1016/0040-1951\(80\)90009-8](https://doi.org/10.1016/0040-1951(80)90009-8)

1005 Delavari, M., Dolati, A., Marroni, M., Pandolfi, L., Saccani, E., 2016. Association of MORB
1006 and SSZ Ophiolites Along the Shear Zone Between Coloured Mélange and Bajgan
1007 Complexes (north Makran, Iran): Evidence from the Sorkhband Area. *Ophioliti*.
1008 <https://doi.org/10.4454/ofioliti.v41i1.440>

1009 Dick, H.J.B., Bullen, T., 1984. Chromian spinel as a petrogenetic indicator in abyssal and
1010 alpine-type peridotites and spatially associated lavas. *Contributions to Mineralogy and*
1011 *Petrology* 86, 54–76. <https://doi.org/10.1007/BF00373711>

1012 Dilek, Y., Furnes, H., Shallo, M., 2008. Geochemistry of the Jurassic Mirdita Ophiolite
1013 (Albania) and the MORB to SSZ evolution of a marginal basin oceanic crust. *Lithos* 100,
1014 174–209. <https://doi.org/10.1016/j.lithos.2007.06.026>

1015 Droop, G.T.R., 1987. A General Equation for Estimating Fe^{3+} Concentrations in
1016 Ferromagnesian Silicates and Oxides from Microprobe Analyses, Using Stoichiometric
1017 Criteria. *Mineralogical Magazine* 51, 431–435.
1018 <https://doi.org/10.1180/minmag.1987.051.361.10>

1019 Dupré, B., Allègre, C.J., 1983. Pb–Sr isotope variation in Indian Ocean basalts and mixing
1020 phenomena. *Nature* 303, 142–146. <https://doi.org/10.1038/303142a0>

1021 El Shazly, A.E.-D.K., Bröcker, M., Hacker, B.R., Calvert, A.J., 2001. Formation and
1022 exhumation of blueschists and eclogites from NE Oman: new perspectives from Rb–Sr and
1023 $^{40}\text{Ar}/^{39}\text{Ar}$ dating. *Journal of Metamorphic Geology* 19, 233–248.
1024 <https://doi.org/10.1046/j.1525-1314.2001.00309.x>

1025 Faccenna, C., Becker, T.W., Auer, L., Billi, A., Boschi, L., Brun, J.P., Capitanio, F.A.,
1026 Funicello, F., Horvath, F., Jolivet, L., Piromallo, C., Royden, L., Rossetti, F., Serpelloni, E.,
1027 2014. Mantle dynamics in the Mediterranean. *Reviews of Geophysics* 52, 283–332.
1028 <https://doi.org/10.1002/2013RG000444>

1029 Frey, F.A., Weis, D., 1995. Temporal evolution of the kerguelen plume: Geochemical
1030 evidence from 38 to 82 ma lavas forming the Ninetyeast ridge. *Contributions to Mineralogy*
1031 *and Petrology* 121, 12–28. <https://doi.org/10.1007/s004100050087>

1032 Gansser, A., 1960. Ausseralpine Ophiolothprobleme. *Eclogae Geologicae Helveticae* 52, 659–
1033 680.

1034 Gao, J., John, T., Klemd, R., Xiong, X., 2007. Mobilization of Ti–Nb–Ta during subduction:
1035 Evidence from rutile-bearing dehydration segregations and veins hosted in eclogite, Tianshan,
1036 NW China. *Geochimica et Cosmochimica Acta* 71, 4974–4996.
1037 <https://doi.org/10.1016/j.gca.2007.07.027>

1038 Gharib, F., De Wever, P., 2010. Radiolaires Mésozoïques de la formation de Kermanshah
1039 (Iran). *Comptes Rendus Palevol* 9, 209–219. <https://doi.org/10.1016/j.crpv.2010.06.003>

1040 Ghasemi, A., Talbot, C.J., 2006. A new tectonic scenario for the Sanandaj–Sirjan Zone (Iran).
1041 *Journal of Asian Earth Sciences* 26, 683–693. <https://doi.org/10.1016/j.jseaes.2005.01.003>

1042 Ghasemi, H., Juteau, T., Bellon, H., Sabzehei, M., Whitechurch, H., Ricou, L.-E., 2002. The
1043 mafic–ultramafic complex of Sikhoran (central Iran): a polygenetic ophiolite complex.

1044 Comptes Rendus Geoscience 334, 431–438. [https://doi.org/10.1016/S1631-0713\(02\)01770-4](https://doi.org/10.1016/S1631-0713(02)01770-4)
1045 Ghazi, A.M., Hassanipak, A.A., Mahoney, J.J., Duncan, R.A., 2004. Geochemical
1046 characteristics, ⁴⁰Ar–³⁹Ar ages and original tectonic setting of the Band-e-Zeyarat/Dar Anar
1047 ophiolite, Makran accretionary prism, S.E. Iran. *Tectonophysics* 393, 175–196.
1048 <https://doi.org/10.1016/j.tecto.2004.07.035>
1049 Gillis, K.M., 1995. Controls on hydrothermal alteration in a section of fast-spreading oceanic
1050 crust. *Earth and Planetary Science Letters* 134, 473–489. [https://doi.org/10.1016/0012-](https://doi.org/10.1016/0012-821X(95)00137-2)
1051 [821X\(95\)00137-2](https://doi.org/10.1016/0012-821X(95)00137-2)
1052 Gnos, E., Peters, T., 1993. K-Ar ages of the metamorphic sole of the Semail Ophiolite:
1053 implications for ophiolite cooling history. *Contributions to Mineralogy and Petrology* 113,
1054 325–332. <https://doi.org/10.1007/BF00286925>
1055 Godard, M., Bosch, D., Einaudi, F., 2006. A MORB source for low-Ti magmatism in the
1056 Semail ophiolite. *Chemical Geology* 234, 58–78.
1057 <https://doi.org/10.1016/j.chemgeo.2006.04.005>
1058 Godard, M., Dautria, J.M., Perrin, M., 2003. Geochemical variability of the Oman ophiolite
1059 lavas: Relationship with spatial distribution and paleomagnetic directions. *Geochemistry,*
1060 *Geophysics, Geosystems* 4. <https://doi.org/10.1029/2002GC000452>
1061 Goodenough, K.M., Styles, M.T., Schofield, D., Thomas, R.J., Crowley, Q.C., Lilly, R.M.,
1062 McKervey, J., Stephenson, D., Carney, J.N., 2010. Architecture of the Oman–UAE ophiolite:
1063 evidence for a multi-phase magmatic history. *Arabian Journal of Geosciences* 3, 439–458.
1064 <https://doi.org/10.1007/s12517-010-0177-3>
1065 Guilmette, C., Smit, M.A., van Hinsbergen, D.J.J., Güreş, D., Corfu, F., Charette, B.,
1066 Maffione, M., Rabeau, O., Savard, D., 2018. Forced subduction initiation recorded in the sole
1067 and crust of the Semail Ophiolite of Oman. *Nature Geoscience* 11, 688–695.
1068 <https://doi.org/10.1038/s41561-018-0209-2>
1069 Haase, K.M., Freund, S., Koepke, J., Hauff, F., Erdmann, M., 2015. Melts of sediments in the
1070 mantle wedge of the Oman ophiolite. *Geology* 43, 275–278. <https://doi.org/10.1130/G36451.1>
1071 Hacker, B.R., Mosenfelder, J.L., Gnos, E., 1996. Rapid emplacement of the Oman ophiolite:
1072 Thermal and geochronologic constraints. *Tectonics* 15, 1230–1247.
1073 <https://doi.org/10.1029/96TC01973>
1074 Hassanzadeh, J., Wernicke, B.P., 2016. The Neotethyan Sanandaj-Sirjan zone of Iran as an
1075 archetype for passive margin-arc transitions. *Tectonics* 35, 586–621.
1076 <https://doi.org/10.1002/2015TC003926>
1077 Hastie, A.R., Kerr, A.C., Pearce, J.A., Mitchell, S.F., 2007. Classification of Altered Volcanic
1078 Island Arc Rocks using Immobile Trace Elements: Development of the Th–Co Discrimination
1079 Diagram. *Journal of Petrology* 48, 2341–2357. <https://doi.org/10.1093/petrology/egm062>
1080 Hauff, F., Hoernle, K., Schmidt, A., 2003. Sr-Nd-Pb composition of Mesozoic Pacific oceanic
1081 crust (Site 1149 and 801, ODP Leg 185): Implications for alteration of ocean crust and the
1082 input into the Izu-Bonin-Mariana subduction system: SR-ND-PB COMPOSITION OF
1083 MESOZOIC PACIFIC. *Geochem. Geophys. Geosyst.* 4.
1084 <https://doi.org/10.1029/2002GC000421>
1085 Hauff, F., Hoernle, K., Schmincke, H.-U., Werner, R., 1997. A Mid Cretaceous origin for the
1086 Galápagos hotspot: volcanological, petrological and geochemical evidence from Costa Rican
1087 oceanic crustal segments. *Geologische Rundschau* 86, 141–155.
1088 <https://doi.org/10.1007/PL00009938>
1089 Hawkins, J.W., Bloomer, S.H., Evans, C.A., Melchior, J.T., 1984. Evolution of intra-oceanic
1090 arc-trench systems. *Tectonophysics* 102, 175–205. [https://doi.org/10.1016/0040-](https://doi.org/10.1016/0040-1951(84)90013-1)
1091 [1951\(84\)90013-1](https://doi.org/10.1016/0040-1951(84)90013-1)
1092 Hémond, C., Hofmann, A.W., Vlastélic, I., Nauret, F., 2006. Origin of MORB enrichment
1093 and relative trace element compatibilities along the Mid-Atlantic Ridge between 10° and

1094 24°N. *Geochemistry, Geophysics, Geosystems* 7, n/a-n/a.
1095 <https://doi.org/10.1029/2006GC001317>
1096 Hochstaedter, A., Gill, J., Peters, R., Broughton, P., Holden, P., Taylor, B., 2001. Across-arc
1097 geochemical trends in the Izu-Bonin arc: Contributions from the subducting slab.
1098 *Geochemistry, Geophysics, Geosystems* 2. <https://doi.org/10.1029/2000GC000105>
1099 Humphris, S.E., Thompson, G., 1978. Trace element mobility during hydrothermal alteration
1100 of oceanic basalts. *Geochimica et Cosmochimica Acta* 42, 127–136.
1101 [https://doi.org/10.1016/0016-7037\(78\)90222-3](https://doi.org/10.1016/0016-7037(78)90222-3)
1102 Hunziker, D., Burg, J.-P., Bouilhol, P., von Quadt, A., 2015. Jurassic rifting at the Eurasian
1103 Tethys margin: Geochemical and geochronological constraints from granitoids of North
1104 Makran, southeastern Iran. *Tectonics* 34, 571–593. <https://doi.org/10.1002/2014TC003768>
1105 Hunziker, D., Burg, J.-P., Moulas, E., Reusser, E., Omrani, J., 2017. Formation and
1106 preservation of fresh lawsonite: Geothermobarometry of the North Makran Blueschists,
1107 southeast Iran. *Journal of Metamorphic Geology* 35, 871–895.
1108 <https://doi.org/10.1111/jmg.12259>
1109 Ishikawa, T., Fujisawa, S., Nagaishi, K., Masuda, T., 2005. Trace element characteristics of
1110 the fluid liberated from amphibolite-facies slab: Inference from the metamorphic sole beneath
1111 the Oman ophiolite and implication for boninite genesis. *Earth and Planetary Science Letters*
1112 240, 355–377. <https://doi.org/10.1016/j.epsl.2005.09.049>
1113 Ishikawa, T., Nagaishi, K., Umino, S., 2002. Boninitic volcanism in the Oman ophiolite:
1114 Implications for thermal condition during transition from spreading ridge to arc. *Geology* 30,
1115 899–902. [https://doi.org/10.1130/0091-7613\(2002\)030<0899:BVITOO>2.0.CO;2](https://doi.org/10.1130/0091-7613(2002)030<0899:BVITOO>2.0.CO;2)
1116 Ishizuka, O., Tani, K., Reagan, M.K., Kanayama, K., Umino, S., Harigane, Y., Sakamoto, I.,
1117 Miyajima, Y., Yuasa, M., Dunkley, D.J., 2011. The timescales of subduction initiation and
1118 subsequent evolution of an oceanic island arc. *Earth and Planetary Science Letters* 306, 229–
1119 240. <https://doi.org/10.1016/j.epsl.2011.04.006>
1120 Jafari, A., Fazlnia, A., Jamei, S., 2018. Geochemistry, petrology and geodynamic setting of
1121 the Urumieh plutonic complex, Sanandaj–Sirjan zone, NW Iran: New implication for Arabian
1122 and Central Iranian plate collision. *Journal of African Earth Sciences* 139, 421–439.
1123 <https://doi.org/10.1016/j.jafrearsci.2017.11.039>
1124 Jannessary, M.R., 2003. Les ophiolites de Neyriz (Sud de l’Iran) : Naissance d’une dorsale en
1125 pied de marge continentale (étude des structures internes, de la fabrication du manteau, et de
1126 l’évolution pétro-géochimique des magmas) (PhD thesis). Université Louis Pasteur,
1127 Strasbourg.
1128 Jannessary, M.R., Whitechurch, H., 2008. The birth of an oceanic crust at the foot of Gond-
1129 wana margin (Neyriz ophiolite, Iran). *Geosciences* 17, 41–48.
1130 John, T., Scherer, E.E., Schenk, V., Herms, P., Halama, R., Garbe-Schönberg, C.-D., 2010.
1131 Subducted seamounts in an eclogite-facies ophiolite sequence: the Andean Raspas Complex,
1132 SW Ecuador. *Contributions to Mineralogy and Petrology* 159, 265–284.
1133 <https://doi.org/10.1007/s00410-009-0427-0>
1134 Kananian, A., Juteau, T., Bellon, H., Darvishzadeh, A., Sabzehi, M., Whitechurch, H., Ricou,
1135 L.-E., 2001. The ophiolite massif of Kahnij (western Makran, southern Iran): new geological
1136 and geochronological data. *Comptes Rendus de l’Académie des Sciences - Series IIA - Earth
1137 and Planetary Science* 332, 543–552. [https://doi.org/10.1016/S1251-8050\(01\)01574-9](https://doi.org/10.1016/S1251-8050(01)01574-9)
1138 Kawahata, H., Nohara, M., Ishizuka, H., Hasebe, S., Chiba, H., 2001. Sr isotope geochemistry
1139 and hydrothermal alteration of the Oman ophiolite. *J. Geophys. Res.* 106, 11083–11099.
1140 <https://doi.org/10.1029/2000JB900456>
1141 Khalatbari-Jafari, M., Juteau, T., Bellon, H., Whitechurch, H., Cotten, J., Emami, H., 2004.
1142 New geological, geochronological and geochemical investigations on the Khoy ophiolites and
1143 related formations, NW Iran. *Journal of Asian Earth Sciences* 23, 507–535.

1144 <https://doi.org/10.1016/j.jseaes.2003.07.005>

1145 König, S., Münker, C., Schuth, S., Luguet, A., Hoffmann, J.E., Kuduon, J., 2010. Boninites as
1146 windows into trace element mobility in subduction zones. *Geochimica et Cosmochimica Acta*
1147 74, 684–704. <https://doi.org/10.1016/j.gca.2009.10.011>

1148 Kusano, Y., Hayashi, M., Adachi, Y., Umino, S., Miyashita, S., 2014. Evolution of volcanism
1149 and magmatism during initial arc stage: constraints on the tectonic setting of the Oman
1150 Ophiolite. Geological Society, London, Special Publications 392, 177–193.
1151 <https://doi.org/10.1144/SP392.9>

1152 Kusano, Y., Umino, S., Shinjo, R., Ikei, A., Adachi, Y., Miyashita, S., Arai, S., 2017.
1153 Contribution of slab-derived fluid and sedimentary melt in the incipient arc magmas with
1154 development of the paleo-arc in the Oman Ophiolite. *Chemical Geology* 449, 206–225.
1155 <https://doi.org/10.1016/j.chemgeo.2016.12.012>

1156 Lachize, M., Lorand, J.P., Juteau, T., 1996. Calc-alkaline differentiation trend in the plutonic
1157 sequence of the Wadi Haymiliyah section, Haylayn massif, Semail ophiolite, Oman. *Lithos*
1158 38, 207–232. [https://doi.org/10.1016/0024-4937\(96\)00009-6](https://doi.org/10.1016/0024-4937(96)00009-6)

1159 Lanphere, M.A., Pamić, J., 1983. Ages and tectonic setting of ophiolite from the Neyriz area,
1160 southeast Zagros Range, Iran. *Tectonophysics* 96, 245–256. [https://doi.org/10.1016/0040-](https://doi.org/10.1016/0040-1951(83)90220-2)
1161 [1951\(83\)90220-2](https://doi.org/10.1016/0040-1951(83)90220-2)

1162 Lapiere, H., 2004. The Tethyan plume: geochemical diversity of Middle Permian basalts
1163 from the Oman rifted margin. *Lithos* 74, 167–198.
1164 <https://doi.org/10.1016/j.lithos.2004.02.006>

1165 Leterrier, J., Maury, R.C., Thonon, P., Girard, D., Marchal, M., 1982. Clinopyroxene
1166 composition as a method of identification of the magmatic affinities of paleo-volcanic series.
1167 *Science* 59, 139–154.

1168 Lippard, S.J., Shelton, A.W., Gass, I.G., 1986. The ophiolite of Northern Oman, The
1169 Geological Society. ed.

1170 Liu, Y., Gao, S., Hu, Z., Gao, C., Zong, K., Wang, D., 2010. Continental and Oceanic Crust
1171 Recycling-induced Melt-Peridotite Interactions in the Trans-North China Orogen: U-Pb
1172 Dating, Hf Isotopes and Trace Elements in Zircons from Mantle Xenoliths. *Journal of*
1173 *Petrology* 51, 537–571. <https://doi.org/10.1093/petrology/egp082>

1174 Liu, Y., Hu, Z., Gao, S., Günther, D., Xu, J., Gao, C., Chen, H., 2008. In situ analysis of
1175 major and trace elements of anhydrous minerals by LA-ICP-MS without applying an internal
1176 standard. *Chemical Geology* 257, 34–43. <https://doi.org/10.1016/j.chemgeo.2008.08.004>

1177 Ludwig, K.R., 2001. Users Manual for Isoplot/Ex.: A Geochronological Toolkit for Microsoft
1178 Excel.

1179 MacPherson, G.T., 1983. The Snow Mountain Volcanic Complex: an on-land seamount in the
1180 Franciscan Terrain, California. *Journal of Geology* 91, 73–92.

1181 Madjidi, B., Berberian, M., Hushmandzadeh, A., Nowgole-Sadat, M.A.A., Sabzehei, M.,
1182 Alavi-Tehrani, N., Azizan, H., Nazemzadeh, M., Roshan ravan-H, J., Afaghe, A.,
1183 Afsharianzadeh, A.M., Dehaghe, F., Ghomashi, A., 1993. Geological Map of Iran, 1 :
1184 250000 series - Haji Abad.

1185 Malavieille, J., Lallemand, S.E., Dominguez, S., Deschamps, A., Lu, C.-Y., Liu, C.-S.,
1186 Schnuerle, P., Angelier, J., Collot, J.Y., Deffontaines, B., Fournier, M., Hsu, S.K., Le Formal,
1187 J.P., Liu, S.Y., Sibuet, J.C., Thureau, N., Wang, F., the ACT (Active Collision in Taiwan)
1188 Scientific Crew, 2002. Arc-continent collision in Taiwan: New marine observations and
1189 tectonic evolution, in: Special Paper 358: Geology and Geophysics of an Arc-Continent
1190 Collision, Taiwan. Geological Society of America, pp. 187–211. [https://doi.org/10.1130/0-](https://doi.org/10.1130/0-8137-2358-2.187)
1191 [8137-2358-2.187](https://doi.org/10.1130/0-8137-2358-2.187)

1192 Martin, H., 1999. Adakitic magmas: Modern analogues of Archaean granitoids. *Lithos* 46,
1193 411–429. [https://doi.org/10.1016/S0024-4937\(98\)00076-0](https://doi.org/10.1016/S0024-4937(98)00076-0)

1194 McCall, G.J.H., 1997. The geotectonic history of the Makran and adjacent areas of southern
1195 Iran. *Journal of Asian Earth Sciences* 15, 517–531. [https://doi.org/10.1016/S0743-](https://doi.org/10.1016/S0743-9547(97)00032-9)
1196 9547(97)00032-9

1197 McCulloch, M.T., Gregory, R.T., Wasserburg, G.J., Taylor, H.P., 1981. Sm-Nd, Rb-Sr, and
1198 $^{18}\text{O}/^{16}\text{O}$ isotopic systematics in an oceanic crustal section: Evidence from the Samail
1199 Ophiolite. *Journal of Geophysical Research: Solid Earth* 86, 2721–2735.
1200 <https://doi.org/10.1029/JB086iB04p02721>

1201 Michael, P., 1995. Regionally distinctive sources of depleted MORB: Evidence from trace
1202 elements and H_2O . *Earth and Planetary Science Letters* 131, 301–320.
1203 [https://doi.org/10.1016/0012-821X\(95\)00023-6](https://doi.org/10.1016/0012-821X(95)00023-6)

1204 Moghadam, H.S., Bröcker, M., Griffin, W.L., Li, X.H., Chen, R.-X., O'Reilly, S.Y., 2017.
1205 Subduction, high-P metamorphism, and collision fingerprints in South Iran: Constraints from
1206 zircon U-Pb and mica Rb-Sr geochronology. *Geochemistry, Geophysics, Geosystems* 18,
1207 306–332. <https://doi.org/10.1002/2016GC006585>

1208 Moghadam, H.S., Corfu, F., Chiaradia, M., Stern, R.J., Ghorbani, G., 2014a. Sabzevar
1209 Ophiolite, NE Iran: Progress from embryonic oceanic lithosphere into magmatic arc
1210 constrained by new isotopic and geochemical data. *Lithos* 210–211, 224–241.
1211 <https://doi.org/10.1016/j.lithos.2014.10.004>

1212 Moghadam, H.S., Corfu, F., Stern, R.J., 2013a. U–Pb zircon ages of Late Cretaceous Nain
1213 Dehshir ophiolites, central Iran. *Journal of the Geological Society, London* 170, 175–184.
1214 <https://doi.org/10.1144/jgs2012-066.U>

1215 Moghadam, H.S., Mosaddegh, H., Santosh, M., 2013b. Geochemistry and petrogenesis of the
1216 Late Cretaceous Haji-Abad ophiolite (Outer Zagros Ophiolite Belt, Iran): Implications for
1217 geodynamics of the Bitlis-Zagros suture zone. *Geological Journal* 48, 579–602.
1218 <https://doi.org/10.1002/gj.2458>

1219 Moghadam, H.S., Stern, R.J., 2015. Ophiolites of Iran: Keys to understanding the tectonic
1220 evolution of SW Asia: (II) Mesozoic ophiolites. *Journal of Asian Earth Sciences* 100, 31–59.
1221 <https://doi.org/10.1016/j.jseaes.2014.12.016>

1222 Moghadam, H.S., Stern, R.J., Chiaradia, M., Rahgoshay, M., 2013c. Geochemistry and
1223 tectonic evolution of the Late Cretaceous Gogher–Baft ophiolite, central Iran. *Lithos* 168–
1224 169, 33–47. <https://doi.org/10.1016/j.lithos.2013.01.013>

1225 Moghadam, H.S., Stern, R.J., Rahgoshay, M., 2010. The Dehshir ophiolite (central Iran):
1226 Geochemical constraints on the origin and evolution of the Inner Zagros ophiolite belt.
1227 *Geological Society of America Bulletin* 122, 1516–1547. <https://doi.org/10.1130/B30066.1>

1228 Moghadam, H.S., Whitechurch, H., Rahgoshay, M., Monsef, I., 2009. Significance of Nain-
1229 Baft ophiolitic belt (Iran): Short-lived, transtensional Cretaceous back-arc oceanic basins over
1230 the Tethyan subduction zone. *Comptes Rendus Geoscience* 341, 1016–1028.
1231 <https://doi.org/10.1016/j.crte.2009.06.011>

1232 Moghadam, H.S., Zaki Khedr, M., Chiaradia, M., Stern, R.J., Bakhshizad, F., Arai, S., Ottley,
1233 C.J., Tamura, A., 2014b. Supra-subduction zone magmatism of the Neyriz ophiolite, Iran:
1234 constraints from geochemistry and Sr-Nd-Pb isotopes. *International Geology Review* 56,
1235 1395–1412. <https://doi.org/10.1080/00206814.2014.942391>

1236 Mohammadi, A., Burg, J.-P., Guillong, M., von Quadt, A., 2017. Arc magmatism witnessed
1237 by detrital zircon U-Pb geochronology, Hf isotopes and provenance analysis of Late
1238 Cretaceous-Miocene sandstones of onshore western Makran (SE Iran). *American Journal of*
1239 *Science* 317, 941–964. <https://doi.org/10.2475/08.2017.03>

1240 Moll, M., Paulick, H., Suhr, G., Bach, W., 2007. Data report: microprobe analyses of primary
1241 phases (olivine, pyroxene, and spinel) and alteration products (serpentine, iowaite, talc,
1242 magnetite, and sulfides) in Holes 1268A, 1272A, and 1274A, in: *Proceedings of the Ocean*
1243 *Drilling Program, Scientific Results*. Ocean Drilling Program College Station, TX, pp. 1–13.

1244 Monié, P., Agard, P., 2009. Coeval blueschist exhumation along thousands of kilometers:
1245 Implications for subduction channel processes. *Geochemistry Geophysics Geosystems* 10.
1246 <https://doi.org/10.1029/2009GC002428>

1247 Monsef, I., Monsef, R., Mata, J., Zhang, Z., Pirouz, M., Rezaeian, M., Esmaceli, R., Xiao, W.,
1248 2018a. Evidence for an early-MORB to fore-arc evolution within the Zagros suture zone:
1249 Constraints from zircon U-Pb geochronology and geochemistry of the Neyriz ophiolite (South
1250 Iran). *Gondwana Research* 62, 287–305. <https://doi.org/10.1016/j.gr.2018.03.002>

1251 Monsef, I., Rahgoshay, M., Pirouz, M., Chiaradia, M., Grégoire, M., Ceuleneer, G., 2018b.
1252 The Eastern Makran Ophiolite (SE Iran): evidence for a Late Cretaceous fore-arc oceanic
1253 crust. *International Geology Review* 1–27. <https://doi.org/10.1080/00206814.2018.1507764>

1254 Morris, A., Meyer, M., Anderson, M.W., MacLeod, C.J., 2016. Clockwise rotation of the
1255 entire Oman ophiolite occurred in a suprasubduction zone setting. *Geology* 44, 1055–1058.
1256 <https://doi.org/10.1130/G38380.1>

1257 Nazemzadeh, M., Rashidi, A., Navazi, M., Poshtkuhi, M., Davari, M., Ezatian, F., Sabzehei,
1258 M., Atapour, H., Haddadan, M., 2007. Geological Map of Iran, 1 : 100000 series - Dehsard
1259 (Bazar).

1260 Niu, Y., Collerson, K.D., Batiza, R., Wendt, J.I., Regelous, M., 1999. Origin of enriched-type
1261 mid-ocean ridge basalt at ridges far from mantle plumes: The East Pacific Rise at 11°20'N.
1262 *Journal of Geophysical Research: Solid Earth* 104, 7067–7087.
1263 <https://doi.org/10.1029/1998JB900037>

1264 Omrani, J., Agard, P., Whitechurch, H., Benoit, M., Prouteau, G., Jolivet, L., 2008. Arc-
1265 magmatism and subduction history beneath the Zagros Mountains, Iran: A new report of
1266 adakites and geodynamic consequences. *Lithos* 106, 380–398.
1267 <https://doi.org/10.1016/j.lithos.2008.09.008>

1268 Park, J.-O., Tsuru, T., Kodaira, S., Cummins, P.R., Kaneda, Y., 2002. Splay Fault Branching
1269 Along the Nankai Subduction Zone. *Science* 297, 1157–1160.
1270 <https://doi.org/10.1126/science.1074111>

1271 Patchett, P.J., 1983. Importance of the Lu-Hf isotopic system in studies of planetary
1272 chronology and chemical evolution. *Geochimica et Cosmochimica Acta* 47, 81–91.
1273 [https://doi.org/10.1016/0016-7037\(83\)90092-3](https://doi.org/10.1016/0016-7037(83)90092-3)

1274 Pearce, J.A., 2008. Geochemical fingerprinting of oceanic basalts with applications to
1275 ophiolite classification and the search for Archean oceanic crust. *Lithos* 100, 14–48.
1276 <https://doi.org/10.1016/j.lithos.2007.06.016>

1277 Pearce, J.A., 1996. A users guide to basalt discrimination diagrams. Geological Association of
1278 Canada, Short Course Notes.

1279 Pearce, J.A., Lippard, S.J., Roberts, S., 1984. Characteristics and tectonic significance of
1280 supra-subduction zone ophiolites. Geological Society, London, Special Publications 16, 77–
1281 94. <https://doi.org/10.1144/GSL.SP.1984.016.01.06>

1282 Pearce, J.A., Stern, R.J., Bloomer, S.H., Fryer, P., 2005. Geochemical mapping of the
1283 Mariana arc-basin system: Implications for the nature and distribution of subduction
1284 components. *Geochemistry, Geophysics, Geosystems* 6.
1285 <https://doi.org/10.1029/2004GC000895>

1286 Péron-Pinvidic, G., Manatschal, G., 2009. The final rifting evolution at deep magma-poor
1287 passive margins from Iberia-Newfoundland: a new point of view. *International Journal of*
1288 *Earth Sciences* 98, 1581–1597. <https://doi.org/10.1007/s00531-008-0337-9>

1289 Pirnia, T., Saccani, E., Torabi, G., Chiari, M., Goričan, Š., Barbero, E., 2019. Cretaceous
1290 tectonic evolution of the Neo-Tethys in Central Iran: Evidence from petrology and age of the
1291 Nain-Ashin ophiolitic basalts. *Geoscience Frontiers* S1674987119300647.
1292 <https://doi.org/10.1016/j.gsf.2019.02.008>

1293 Plank, T., 2005. Constraints from Thorium/Lanthanum on Sediment Recycling at Subduction

1294 Zones and the Evolution of the Continents. *Journal of Petrology* 46, 921–944.
1295 <https://doi.org/10.1093/petrology/egi005>

1296 Plank, T., Langmuir, C.H., 1998. The chemical composition of subducting sediment and its
1297 consequences for the crust and mantle. *Chemical Geology* 145, 325–394.
1298 [https://doi.org/10.1016/S0009-2541\(97\)00150-2](https://doi.org/10.1016/S0009-2541(97)00150-2)

1299 Ranero, C.R., von Huene, R., 2000. Subduction erosion along the Middle America convergent
1300 margin. *Nature* 404, 748–752. <https://doi.org/10.1038/35008046>

1301 Ricou, L.-E., 1974. L'étude géologique de la région de Neyriz (Zagros iranien) et l'évolution
1302 structurale des Zagrides. (PhD thesis). Université d'Orsay.

1303 Ricou, L.-E., Braud, J., Brunn, J.H., 1977. Le Zagros, in: *Livre à La Mémoire de A.F. de*
1304 *Lapparent (1905–1975), Mémoire Hors-Série de La Société Géologique de France.*

1305 Rioux, M., Bowring, S., Kelemen, P., Gordon, S., Dudás, F., Miller, R., 2012. Rapid crustal
1306 accretion and magma assimilation in the Oman-U.A.E. ophiolite: High precision U-Pb zircon
1307 geochronology of the gabbroic crust: OMAN OPHIOLITE ZIRCON GEOCHRONOLOGY.
1308 *Journal of Geophysical Research: Solid Earth* 117, n/a-n/a.
1309 <https://doi.org/10.1029/2012JB009273>

1310 Rioux, M., Bowring, S., Kelemen, P., Gordon, S., Miller, R., Dudás, F., 2013. Tectonic
1311 development of the Samail ophiolite: High-precision U-Pb zircon geochronology and Sm-Nd
1312 isotopic constraints on crustal growth and emplacement. *Journal of Geophysical Research:*
1313 *Solid Earth* 118, 2085–2101. <https://doi.org/10.1002/jgrb.50139>

1314 Rioux, M., Garber, J., Bauer, A., Bowring, S., Searle, M., Kelemen, P., Hacker, B., 2016.
1315 Synchronous formation of the metamorphic sole and igneous crust of the Semail ophiolite:
1316 New constraints on the tectonic evolution during ophiolite formation from high-precision U–
1317 Pb zircon geochronology. *Earth and Planetary Science Letters* 451, 185–195.
1318 <https://doi.org/10.1016/j.epsl.2016.06.051>

1319 Rollinson, H., 2015. Slab and sediment melting during subduction initiation: granitoid dykes
1320 from the mantle section of the Oman ophiolite. *Contributions to Mineralogy and Petrology*
1321 170. <https://doi.org/10.1007/s00410-015-1177-9>

1322 Rossetti, F., Nasrabad, M., Theye, T., Gerdes, A., Monie, P., Lucci, F., Vignaroli, G., 2014.
1323 Adakite differentiation and emplacement in a subduction channel: The late Paleocene
1324 Sabzevar magmatism (NE Iran). *Geological Society of America Bulletin* 126, 317–343.
1325 <https://doi.org/10.1130/B30913.1>

1326 Rossetti, F., Nasrabad, M., Vignaroli, G., Theye, T., Gerdes, A., Razavi, M.H., Vaziri, H.M.,
1327 2010. Early Cretaceous migmatitic mafic granulites from the Sabzevar range (NE Iran):
1328 implications for the closure of the Mesozoic peri-Tethyan oceans in central Iran. *Terra Nova*
1329 22, 26–34. <https://doi.org/10.1111/j.1365-3121.2009.00912.x>

1330 Sabzehei, M., 1974. Les mélanges ophiolitiques de la région d'Esfandagheh (Iran méridional)
1331 - Etude pétrologique et structurale - Interprétation dans le cadre iranien. Université
1332 Scientifique et Médicale de Grenoble.

1333 Saccani, E., Allahyari, K., Beccaluva, L., Bianchini, G., 2013. Geochemistry and petrology of
1334 the Kermanshah ophiolites (Iran): Implication for the interaction between passive rifting,
1335 oceanic accretion, and OIB-type components in the Southern Neo-Tethys Ocean. *Gondwana*
1336 *Research* 24, 392–411. <https://doi.org/10.1016/j.gr.2012.10.009>

1337 Saccani, E., Delavari, M., Dolati, A., Marroni, M., Pandolfi, L., Chiari, M., Barbero, E., 2018.
1338 New insights into the geodynamics of Neo-Tethys in the Makran area: Evidence from age and
1339 petrology of ophiolites from the Coloured Mélange Complex (SE Iran). *Gondwana Research*
1340 62, 306–327. <https://doi.org/10.1016/j.gr.2017.07.013>

1341 Schnur, S.R., Gilbert, L.A., 2012. Detailed volcanostratigraphy of an accreted seamount:
1342 Implications for intraplate seamount formation. *Geochemistry, Geophysics, Geosystems* 13,
1343 1–13. <https://doi.org/10.1029/2012GC004301>

1344 Searle, M., Cox, J., 1999. Tectonic setting, origin, and obduction of the Oman ophiolite.
1345 Geological Society of America Bulletin 111, 104–122.

1346 Searle, M.P., 1980. The metamorphic sheet and underlying volcanic rocks beneath the Semail
1347 ophiolite in the Northern Oman mountains of Arabia.

1348 Searle, M.P., Graham, G.M., 1982. “Oman Exotics”—Oceanic carbonate build-ups associated
1349 with the early stages of continental rifting. *Geology* 10, 43. [https://doi.org/10.1130/0091-7613\(1982\)10<43:OECBAW>2.0.CO;2](https://doi.org/10.1130/0091-7613(1982)10<43:OECBAW>2.0.CO;2)

1350 Searle, M.P., Warren, C.J., Waters, D.J., Parrish, R.R., 2004. Structural evolution,
1351 metamorphism and restoration of the Arabian continental margin, Saih Hatat region, Oman
1352 Mountains. *Journal of Structural Geology* 26, 451–473.
1353 <https://doi.org/10.1016/j.jsg.2003.08.005>

1354 Seifert, K., Gibson, I., Weis, D., Brunotte, D., 1996. Geochemistry of metamorphosed
1355 cumulate gabbros from Hole 900A, Iberia Abyssal Plain, in: Whitmarsh, R.B., Sawyer, D.S.,
1356 Klaus, A., Masson, D.G. (Eds.), *Proceedings of the Ocean Drilling Program*, 149 Scientific
1357 Results, *Proceedings of the Ocean Drilling Program*. Ocean Drilling Program.
1358 <https://doi.org/10.2973/odp.proc.sr.149.1996>

1359 Shahbazi, H., Siebel, W., Pourmoafee, M., Ghorbani, M., Sepahi, A.A., Shang, C.K.,
1360 Vousoughi Abedini, M., 2010. Geochemistry and U–Pb zircon geochronology of the Alvand
1361 plutonic complex in Sanandaj–Sirjan Zone (Iran): New evidence for Jurassic magmatism.
1362 *Journal of Asian Earth Sciences* 39, 668–683. <https://doi.org/10.1016/j.jseaes.2010.04.014>

1363 Shervais, J.W., 1982. TiV plots and the petrogenesis of modern and ophiolitic lavas. *Earth
1364 and Planetary Science Letters* 59, 101–118. [https://doi.org/10.1016/0012-821X\(82\)90120-0](https://doi.org/10.1016/0012-821X(82)90120-0)

1365 Sláma, J., Košler, J., Condon, D.J., Crowley, J.L., Gerdes, A., Hanchar, J.M., Horstwood,
1366 M.S.A., Morris, G.A., Nasdala, L., Norberg, N., Schaltegger, U., Schoene, B., Tubrett, M.N.,
1367 Whitehouse, M.J., 2008. Plešovice zircon — A new natural reference material for U–Pb and
1368 Hf isotopic microanalysis. *Chemical Geology* 249, 1–35.
1369 <https://doi.org/10.1016/j.chemgeo.2007.11.005>

1370 Söderlund, U., Patchett, P.J., Vervoort, J.D., Isachsen, C.E., 2004. The ¹⁷⁶Lu decay constant
1371 determined by Lu–Hf and U–Pb isotope systematics of Precambrian mafic intrusions. *Earth
1372 and Planetary Science Letters* 219, 311–324. [https://doi.org/10.1016/S0012-821X\(04\)00012-3](https://doi.org/10.1016/S0012-821X(04)00012-3)

1373 Soret, M., Agard, P., Dubacq, B., Plunder, A., Yamato, P., 2017. Petrological evidence for
1374 stepwise accretion of metamorphic soles during subduction infancy (Semail ophiolite, Oman
1375 and UAE). *Journal of Metamorphic Geology* 35, 1051–1080.
1376 <https://doi.org/10.1111/jmg.12267>

1377 Spilde, M.N., Brearley, A.J., Papike, J.J., 1993. Alteration of plagioclase and pyroxene
1378 phenocrysts in a fissure fumarole, Valley of Ten Thousand Smokes, Alaska. *American
1379 Mineralogist* 78, 1066–1081.

1380 Staudigel, H., Koppers, A., Lavelle, J.W., Pitcher, T.J., Shank, T.M., 2010. Box 1: Defining
1381 the word “seamount.” *Oceanography* 23, 20–21.

1382 Stern, R.J., Bloomer, S.H., 1992. Subduction zone infancy: Examples from the Eocene Izu-
1383 Bonin-Mariana and Jurassic California arcs. *Geological Society of America Bulletin* 104,
1384 1621–1636. <https://doi.org/10.1007/s13398-014-0173-7.2>

1385 Stern, R.J., Lin, P.-N., Morris, J.D., Jackson, M.C., Fryer, P., Bloomer, S.H., Ito, E., 1990.
1386 Enriched back-arc basin basalts from the northern Mariana Trough: implications for the
1387 magmatic evolution of back-arc basins. *Earth and Planetary Science Letters* 100, 210–225.
1388 [https://doi.org/10.1016/0012-821X\(90\)90186-2](https://doi.org/10.1016/0012-821X(90)90186-2)

1389 Stöcklin, J., 1981. A brief report on the geodynamics of Iran. *Zagros Hindu Kush Himalaya
1390 Geodynamic Evolution* 70–74.

1391 Sun, S.-S., McDonough, W.F., 1989. Chemical and isotopic systematics of oceanic basalts:
1392 implications for mantle composition and processes. Geological Society, London, Special
1393

1394 Publications 42, 313–345. <https://doi.org/10.1144/GSL.SP.1989.042.01.19>

1395 Tiezzi, L.J., Scott, R.B., 1980. Crystal fractionation in a Cumulate Gabbro, Mid-Atlantic

1396 Ridge, 26°N. *Journal of Geophysical Research* 85, 5438.

1397 <https://doi.org/10.1029/JB085iB10p05438>

1398 Tirrul, R., Bell, I.R., Griffis, R.J., Camp, V.E., 1983. The Sistan suture zone of eastern Iran.

1399 *Geological Society of America Bulletin* 94, 134–150. [https://doi.org/10.1130/0016-](https://doi.org/10.1130/0016-7606(1983)94<134)

1400 [7606\(1983\)94<134](https://doi.org/10.1130/0016-7606(1983)94<134)

1401 Umino, S., 2012. Emplacement mechanism of off-axis large submarine lava field from the

1402 Oman Ophiolite. *Journal of Geophysical Research: Solid Earth* 117.

1403 <https://doi.org/10.1029/2012JB009198>

1404 van der Meer, D.G., van Hinsbergen, D.J.J., Spakman, W., 2018. Atlas of the underworld:

1405 Slab remnants in the mantle, their sinking history, and a new outlook on lower mantle

1406 viscosity. *Tectonophysics* 723, 309–448. <https://doi.org/10.1016/j.tecto.2017.10.004>

1407 van Hinsbergen, D.J.J., Maffione, M., Koornneef, L.M.T., Guilmette, C., 2019. Kinematic

1408 and paleomagnetic restoration of the Semail ophiolite (Oman) reveals subduction initiation

1409 along an ancient Neotethyan fracture zone. *Earth and Planetary Science Letters* 518, 183–196.

1410 <https://doi.org/10.1016/j.epsl.2019.04.038>

1411 Vervoort, J.D., Blichert-Toft, J., 1999. Evolution of the depleted mantle: Hf isotope evidence

1412 from juvenile rocks through time. *Geochimica et Cosmochimica Acta* 63, 533–556.

1413 [https://doi.org/10.1016/S0016-7037\(98\)00274-9](https://doi.org/10.1016/S0016-7037(98)00274-9)

1414 Volpe, A.M., Douglas Macdougall, J., Hawkins, J.W., 1988. Lau Basin basalts (LBB): trace

1415 element and SrNd isotopic evidence for heterogeneity in backarc basin mantle. *Earth and*

1416 *Planetary Science Letters* 90, 174–186. [https://doi.org/10.1016/0012-821X\(88\)90099-4](https://doi.org/10.1016/0012-821X(88)90099-4)

1417 Warren, C.J., Parrish, R.R., Waters, D.J., Searle, M.P., 2005. Dating the geologic history of

1418 Oman's Semail ophiolite: insights from U-Pb geochronology. *Contributions to Mineralogy*

1419 *and Petrology* 150, 403–422. <https://doi.org/10.1007/s00410-005-0028-5>

1420 Warren, C.J., Waters, D.J., 2006. Oxidized eclogites and garnet-blueschists from Oman: P-T

1421 path modelling in the NCFMASHO system. *Journal of Metamorphic Geology* 24, 783–802.

1422 <https://doi.org/10.1111/j.1525-1314.2006.00668.x>

1423 Whitechurch, H., Omrani, J., Agard, P., Humbert, F., Montigny, R., Jolivet, L., 2013.

1424 Evidence for Paleocene-Eocene evolution of the foot of the Eurasian margin (Kermanshah

1425 ophiolite, SW Iran) from back-arc to arc: Implications for regional geodynamics and

1426 obduction. *Lithos* 182–183, 11–32. <https://doi.org/10.1016/j.lithos.2013.07.017>

1427 Wood, D.A., 1980. The Application of a Th-Hf-Ta diagrams to problems of tectonomagmatic

1428 classification and to establish the nature of crustal contaminants of basaltic lavas of the British

1429 Tertiary volcanic province. *Earth and Planetary Science Letters* 50, 11–30.

1430 [http://dx.doi.org/10.1016/0012-821X\(80\)90116-8](http://dx.doi.org/10.1016/0012-821X(80)90116-8)

1431 Wrobel-Daveau, J.-C., Ringenbach, J.-C., Tavakoli, S., Ruiz, G.M.H., Masse, P., Frizon de

1432 Lamotte, D., 2010. Evidence for mantle exhumation along the Arabian margin in the Zagros

1433 (Kermanshah area, Iran). *Arabian Journal of Geosciences* 3, 499–513.

1434 <https://doi.org/10.1007/s12517-010-0209-z>

1435 Wu, F.-Y., Yang, Y.-H., Xie, L.-W., Yang, J.-H., Xu, P., 2006. Hf isotopic compositions of

1436 the standard zircons and baddeleyites used in U-Pb geochronology. *Chemical Geology* 234,

1437 105–126. <https://doi.org/10.1016/j.chemgeo.2006.05.003>

1438 Xu, J.-F., Castillo, P.R., 2004. Geochemical and Nd-Pb isotopic characteristics of the

1439 Tethyan asthenosphere: implications for the origin of the Indian Ocean mantle domain.

1440 *Tectonophysics* 393, 9–27. <https://doi.org/10.1016/j.tecto.2004.07.028>

1441 Yamato, P., Agard, P., Goffé, B., de Andrade, V., Vidal, O., Jolivet, L., 2007. New, high-

1442 precision P-T estimates for Oman blueschists: implications for obduction, nappe stacking and

1443 exhumation processes. *Journal of Metamorphic Geology* 25, 657–682.

1444 <https://doi.org/10.1111/j.1525-1314.2007.00722.x>
1445 Zamboni, D., Gazel, E., Ryan, J.G., Cannatelli, C., Lucchi, F., Atlas, Z.D., Trela, J., Mazza,
1446 S.E., De Vivo, B., 2016. Contrasting sediment melt and fluid signatures for magma
1447 components in the Aeolian Arc: Implications for numerical modeling of subduction systems.
1448 *Geochem. Geophys. Geosyst.* 17, 2034–2053. <https://doi.org/10.1002/2016GC006301>
1449 Zarrinkoub, M.H., Pang, K.N., Chung, S.L., Khatib, M.M., Mohammadi, S.S., Chiu, H.Y.,
1450 Lee, H.Y., 2012. Zircon U-Pb age and geochemical constraints on the origin of the Birjand
1451 ophiolite, Sistan suture zone, eastern Iran. *Lithos* 154, 392–405.
1452 <https://doi.org/10.1016/j.lithos.2012.08.007>
1453

1454

1455 Figures:

1456 Fig. 1. Geological context. a) Mesozoic and Cenozoic ophiolites and volcanic arcs along the
1457 Zagros suture zone; b) Detailed zoom of the Hajiabad-Esfandagheh zone, showing the
1458 location of the Siah Kuh unit; c) Paleogeographic map of the Iranian-Omanese Neotethys
1459 during Late Cretaceous. Numbers 1 and 2 indicate two hypotheses for the former location of
1460 the Siah Kuh seamount (see discussion for more details).

1461

1462 Fig. 2. Structural frame: the Siah Kuh seamount (modified after Bonnet et al., 2019). a) Map
1463 of the Siah Kuh unit, the meaning of the color fill for samples is shown on Fig. 2c; b)
1464 Synthetic cross-section of the Siah Kuh seamount; c) Synthetic log of the A and B units, and
1465 proposed correlations (bon. = boninites).

1466

1467 Fig. 3. Field pictures. a) Reef carbonates resting on top of A₁ unit lavas. The granite intrusion
1468 is related to felsic lavas studied hereafter. Rejuvenated magmatism of the A₁' unit above the
1469 limestones; b) Sediment intercalation between the A₁ unit and magmatic rejuvenation in the
1470 A unit (A₃); c) Pillow lavas of the core of the seamount; d) Rhyolite dykes in basalt in the core
1471 of the seamount (A₁ unit); e) Anorthosite dyke intruding serpentinite at the base of the B
1472 unit; f) Structure of the northern B unit.

1473

1474 Fig. 4. Microphotographs of representative rocks from the Siah Kuh seamount, from Unit A
1475 (a-c), Unit B (d-f) and felsic associated rocks from both units (g-i). All pictures are at the same
1476 scale and the white horizontal bar represents 500 μm. a) Porphyric texture of sample 1635;
1477 b) Sample 1746 with a phaneritic texture; c) Porphyric texture of sample 1614b; d) Poikilitic
1478 texture of sample 1532, where zircons have been dated; e) Intergranular texture of sample

1479 1735; f) Porphyric texture of sample 1432 where zircons have been dated; g) Porphyric
1480 texture of sample 1601; h) Trachytic texture of sample 1725; i) Phaneritic texture of sample
1481 1720, where zircons have been dated.

1482 Abbreviations are: Cpx: clinopyroxene, Pl: plagioclase, Chl: chlorite, ex-Pl -> Lws:
1483 replacement of magmatic plagioclase by metamorphic lawsonite, Or: orthoclase, Qz: quartz.

1484

1485 Fig. 5. Classification of rocks based on immobile elements. a) Zr/Ti – Nb/Y diagram after
1486 Pearce (1996); b) Th – Co diagram after Hastie et al. (2007). Siah Kuh boninites after
1487 Moghadam et al. (2013b).

1488

1489 Fig. 6. Rare-earth element and multi-element diagrams for all rocks normalized to chondrite
1490 and primitive mantle respectively (Sun and McDonough, 1989). (a, b) Mafic rocks of the core
1491 of the A unit; (c, d) Felsic rocks of the A and B units; (e, f) Magmatic rejuvenation within the A
1492 unit; (g, h) Mafic rocks of B unit, including Siah Kuh boninites (Moghadam et al., 2013b).
1493 Reference spectra are Oman V2 (Alabaster et al., 1982; Godard et al., 2003) and Oman
1494 boninite (Upper V2, Ishikawa et al., 2005; Kusano et al., 2014).

1495

1496 Fig. 7. Trace element discrimination diagrams of mafic rocks. a) Th/Yb vs Nb/Yb diagram by
1497 Pearce (2008), with a density map of the composition of basalts from present-day
1498 seamounts (including intra-oceanic arc seamounts). GLOSS (global subducting sediment)
1499 values from (Plank and Langmuir, 1998) The scale refers to the number of occurrence in the
1500 Georoc database (<http://georoc.mpch-mainz.gwdg.de>); b) V vs Ti diagram by Shervais
1501 (1982); c) Th-Hf-Ta ternary diagram by Wood (1980); d) Th/La vs Sm/La diagram after Plank
1502 (2005). Siah Kuh boninites after Moghadam et al. (2013b).

1503

1504 Fig. 8. Sr-Nd isotope values for representative rocks of each unit. Cretaceous seawater-rock
1505 mixing line from McCulloch et al. (1981), mixing curve with GLOSS sediment from Plank and
1506 Langmuir (1998). Oman data from Godard et al. (2006), Neyriz from Moghadam et al.
1507 (2014b) and Nain-Baft from Moghadam et al. (2013c).

1508

1509 Fig. 9. Mineral compositions of clinopyroxene and spinel. (a-c) Clinopyroxene discrimination
1510 diagrams in mafic rocks from Leterrier et al. (1982). a) Ti vs Ca + Na diagram showing all

1511 clinopyroxenes plotting in the calc-alkaline to tholeiitic field; b) Ti + Cr vs Ca diagram
1512 showing most of the clinopyroxene analyses from the core of the seamount plotting in the
1513 orogenic basalts field and other mafic rocks in the non-orogenic tholeiite field; c) Ti vs Al
1514 diagram showing that clinopyroxenes from the core of the seamount plot in the arc tholeiite
1515 field (other analyses not plotted); d) Cr# vs Mg# diagram for spinel in ultramafic rocks after
1516 (Dick and Bullen, 1984) showing all analyses plotting in the supra-subduction zone field.

1517

1518 Fig. 10. Wetherill Concordia diagrams for 4 samples and $^{206}\text{Pb}/^{238}\text{U}$ age dispersion plots. a)
1519 Rhyolite within A1 (sample 1518), inset shows a zoom on the 70-110 Ma age window; b)
1520 Anorthosite within B (sample 1720); c) Gabbro within B (sample 1532); d) Basalt at the top of
1521 B (sample 1432), inset shows a zoom on the 70-110 Ma age window. Ages mentioned are
1522 weighted averages (*: youngest zircon population).

1523

1524 Fig. 11. Zircon $\epsilon\text{Hf}(t)$ vs age plot showing positive values for most zircons.

1525

1526 Fig. 12. Synthesis of the tectono-magmatic evolution of the Siah Kuh seamount. a) Two stage
1527 evolution of the Siah Kuh seamount during late Cretaceous; b) hypothesis 1:
1528 Paleogeographic location of the Siah Kuh seamount as a southern intra-Neotethys arc, c)
1529 hypothesis 2: paleogeographic location of the Siah Kuh seamount as an intraoceanic arc in
1530 the northern Neotethys. Abbreviations are San. for Sanandaj-Sirjan, N.B. for Nain-Baft, C.
1531 Iran for Central Iran.

1532

1533 Tables:

1534 Table 1: Sample nature, performed analyses and detailed mineralogy (Gl.= glass).

1535 Table 2: Regional analogs of the Siah Kuh massif in their Neotethyan context: Kermanshah
1536 arc (Whitechurch et al., 2013), Kermanshah ophiolitic complex (Ao et al., 2016; Delaloye and
1537 Desmons, 1980; Gharib and De Wever, 2010; Ricou et al., 1977; Sacconi et al., 2013;
1538 Whitechurch et al., 2013; Wrobel-Daveau et al., 2010), Zagros eclogites (Davoudian et al.,
1539 2008, 2016), Neyriz ophiolitic complex (Babaie et al., 2006, 2001; Jannessary, 2003;
1540 Jannessary and Whitechurch, 2008; Lanphere and Pamić, 1983; Moghadam et al., 2014b;
1541 Monsef et al., 2018a; Ricou, 1974), Siah Kuh unit (Moghadam et al., 2013b, this study), South
1542 Hajiabad ophiolite (Moghadam et al., 2017, 2013b), Zagros blueschists (Agard et al., 2006;

1543 Angiboust et al., 2016; Moghadam et al., 2017; Monié and Agard, 2009), Sikhoran complex
1544 (Ahmadipour et al., 2003; Ghasemi et al., 2002), Sargaz-Abshur complex (Ghasemi et al.,
1545 2002; Sabzehei, 1974), Oman Exotics (Searle and Graham, 1982), Haybi complex (Searle,
1546 1980), Semail ophiolite (Alabaster et al., 1982; Godard et al., 2003; Guilmette et al., 2018;
1547 Hacker et al., 1996; Ishikawa et al., 2005, 2002; Lachize et al., 1996; Rioux et al., 2016, 2013,
1548 2012; Rollinson, 2015; Soret et al., 2017), Oman blueschists (El Shazly et al., 2001; Searle et
1549 al., 2004; Warren et al., 2005; Warren and Waters, 2006; Yamato et al., 2007), Makran
1550 colored mélange (Burg, 2018; Sacconi et al., 2018), Makran blueschists (Delaloye and
1551 Desmons, 1980; Hunziker et al., 2017), Western Iranian Makran (Mohammadi et al., 2017),
1552 Nain-Baft ophiolite (Moghadam et al., 2013a, 2009; Pirnia et al., 2019), Sistan ophiolite
1553 (Babazadeh and de Wever, 2004; Tirrul et al., 1983; Zarrinkoub et al., 2012), Sabzevar
1554 ophiolite (Moghadam et al., 2014a; Rossetti et al., 2014), Sanandaj-Sirjan zone (Arvin et al.,
1555 2007; Jafari et al., 2018; Shahbazi et al., 2010), Urumieh-Dokhtar zone (Omrani et al., 2008)

1556

1557

1558 Supplementary materials

1559 S1: GPS location of samples.

1560 S2: Bulk-rock major and trace element analyses.

1561 S3: Bulk-rock Sr-Nd analyses.

1562 S4: Clinopyroxene EPMA analyses.

1563 S5: Spinel EPMA analyses.

1564 S6: Zircon cathodoluminescence images (concordant)

1565 S7: Zircon U-Pb isotope analyses of concordant zircons.

1566 S8: Zircon trace element data (concordant).

1567 S9: Zircon trace element diagram (concordant).

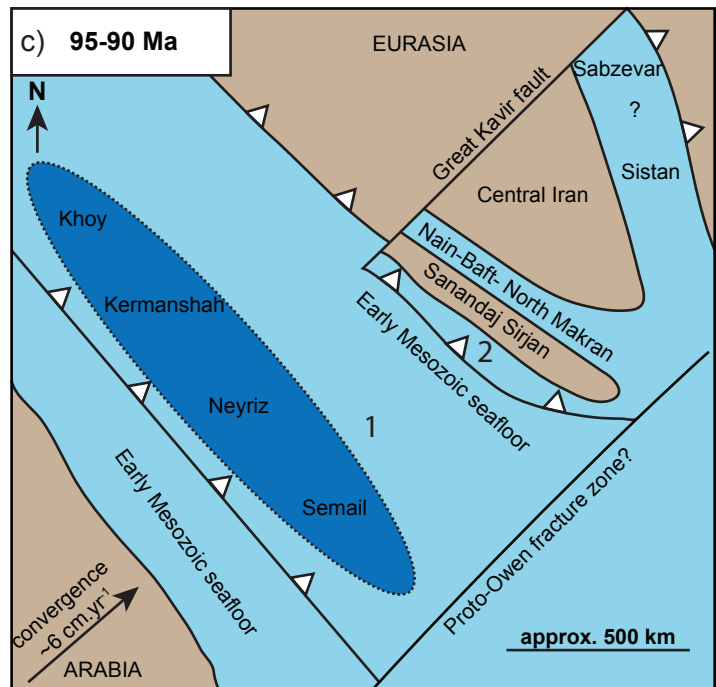
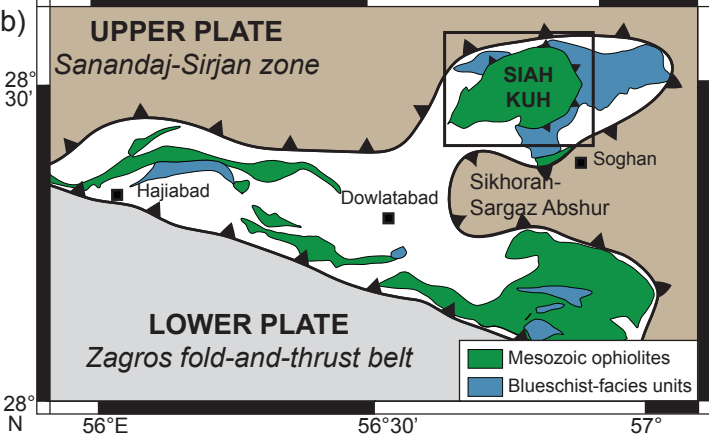
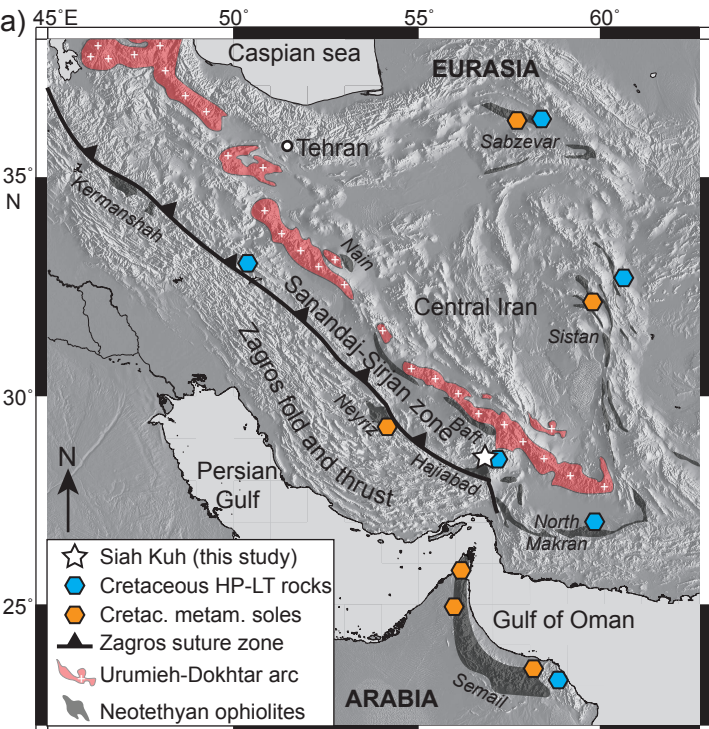
1568 S10: Zircon Lu-Hf isotope analyses of concordant zircons.

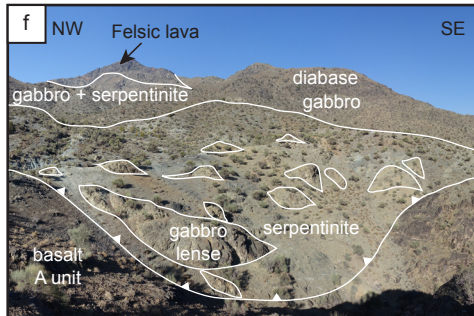
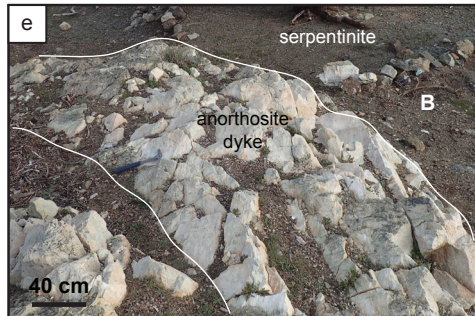
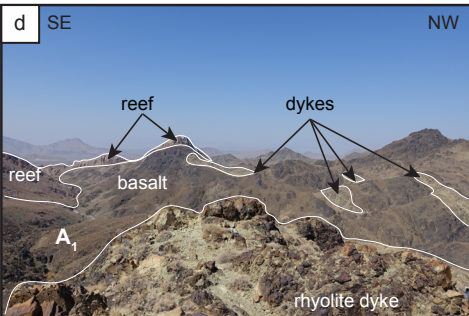
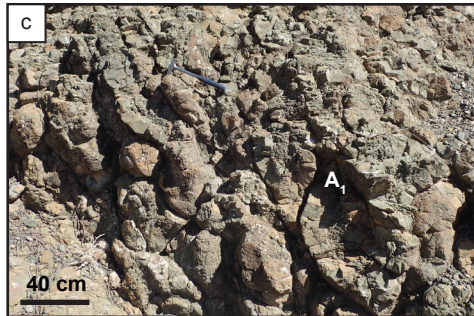
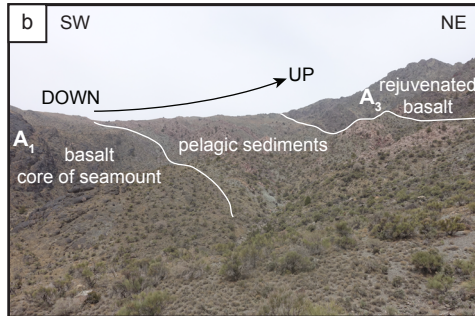
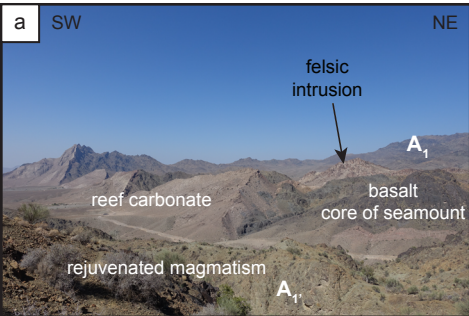
1569 S11: Correlation diagrams between LOI and elements concentrations/isotopic values.

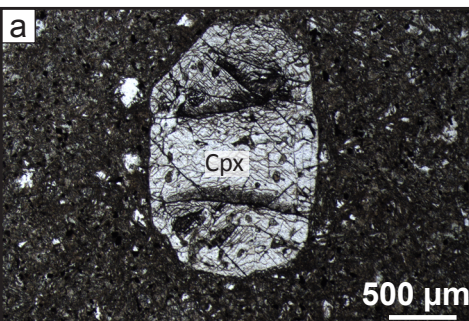
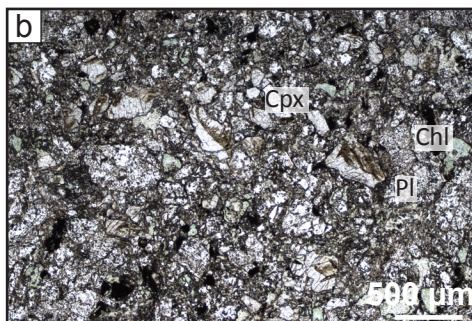
1570 S12: Effect of alteration on Sr isotopic signatures.

1571

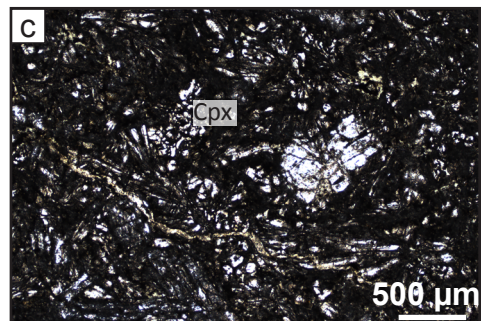
1572



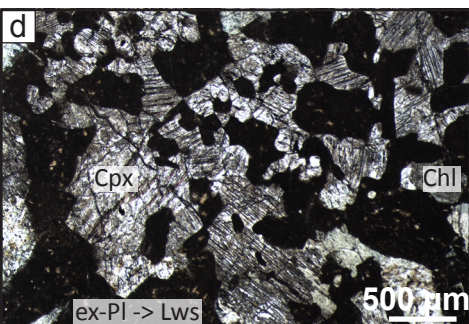


Basalt - core of seamount (A_1)

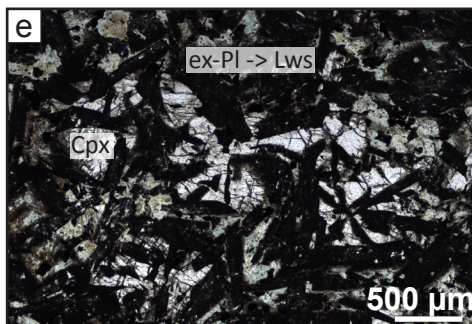
Basalt - early rejuvenation in A



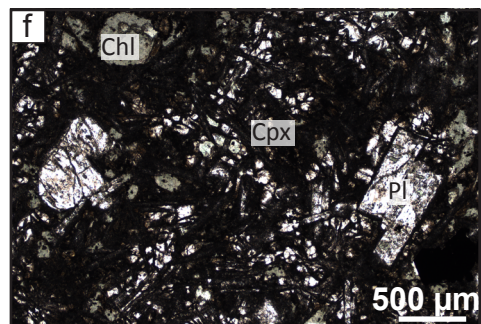
Basalt - late rejuvenation in A



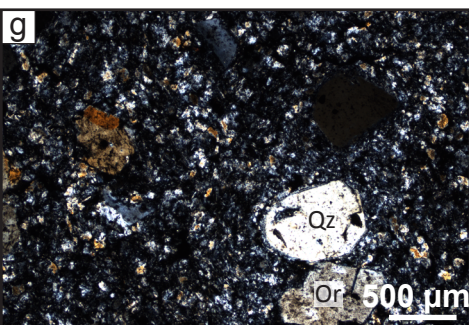
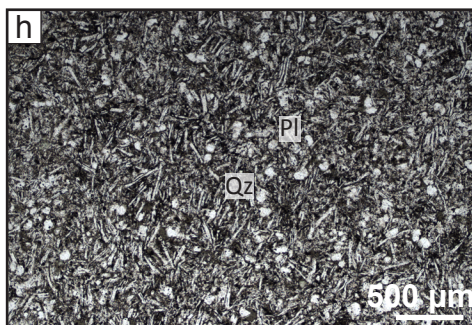
Gabbro - base of B unit



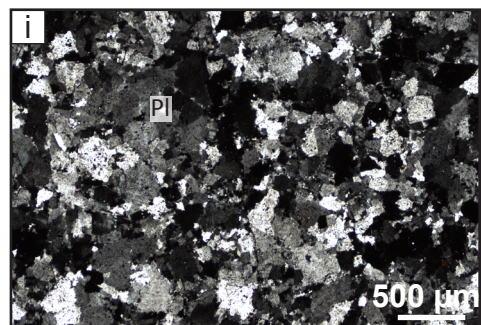
Diabase - base of B unit



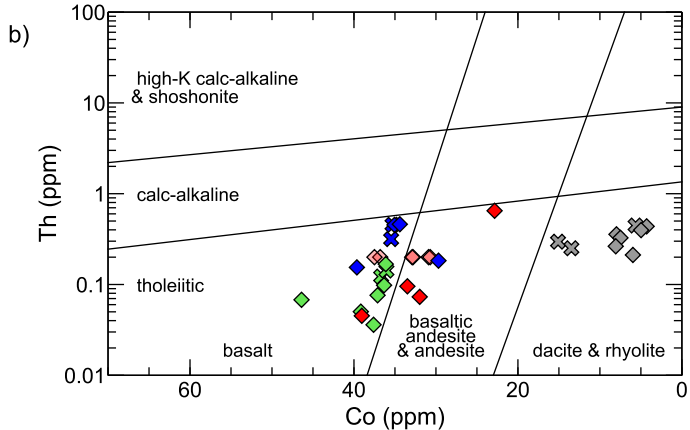
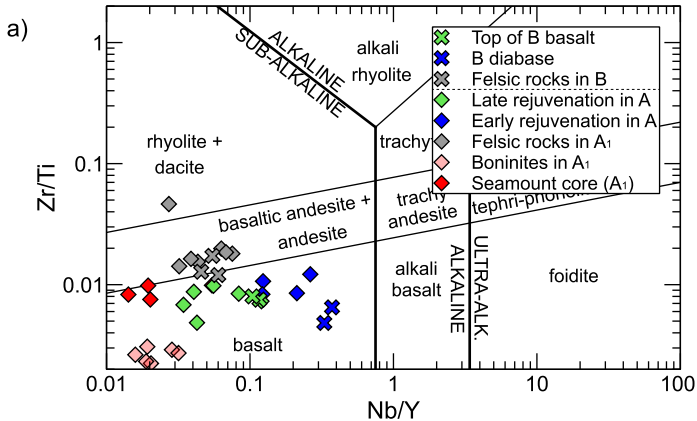
Basalt - top of B unit

Rhyolite - core of seamount (A_1)

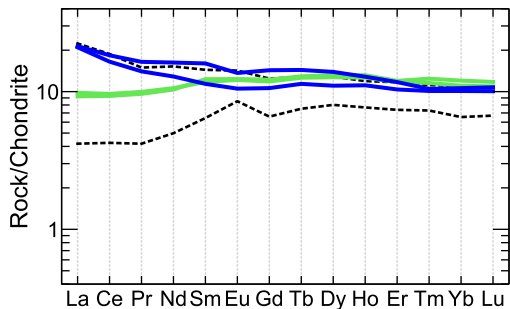
Rhyolite - B unit



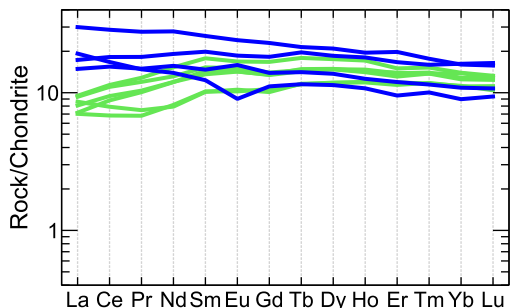
Anorthosite - base of B unit



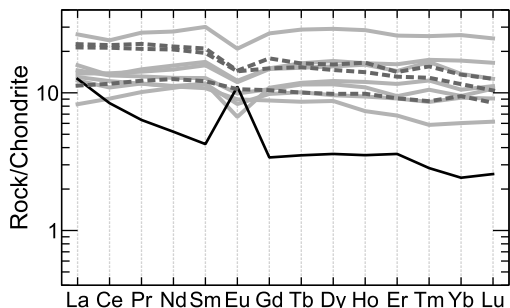
g) Mafic rocks in B



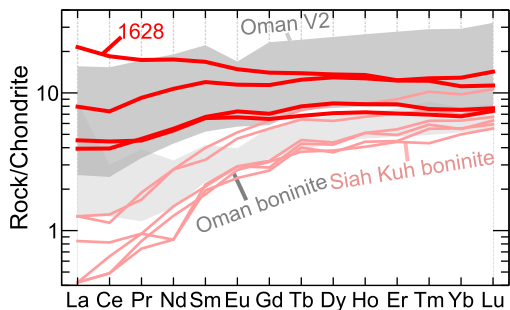
e) Magmatic rejuvenation in A



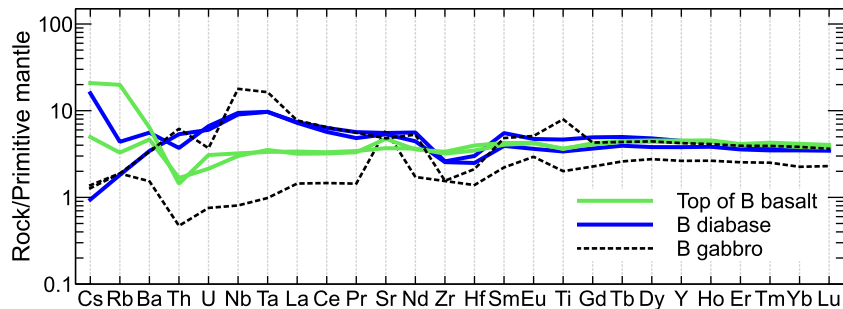
c) Felsic rocks in A and B



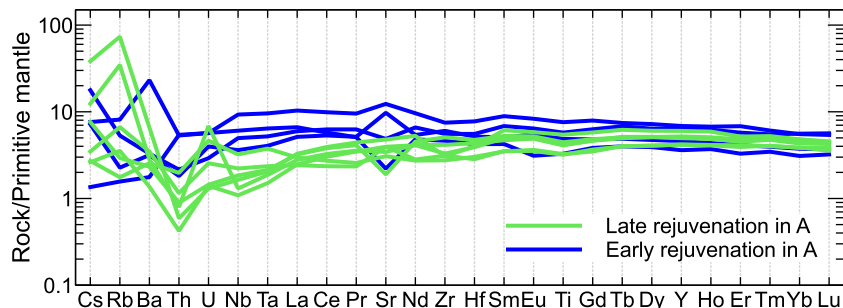
a) Core of A unit basaltic rocks



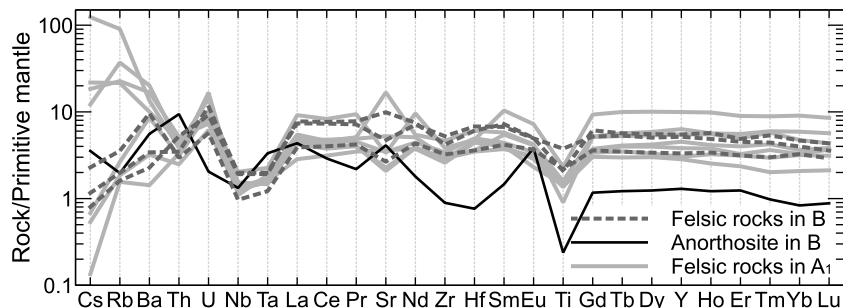
h)



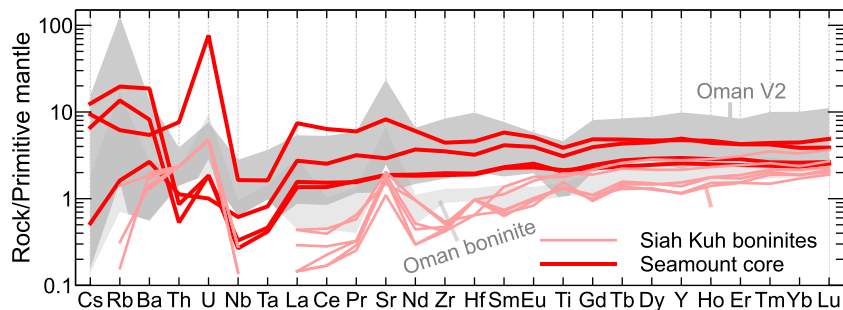
f)



d)



b)



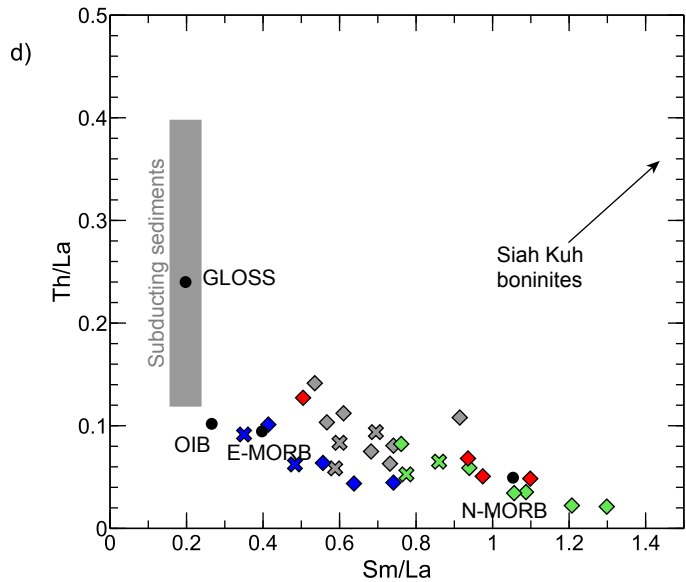
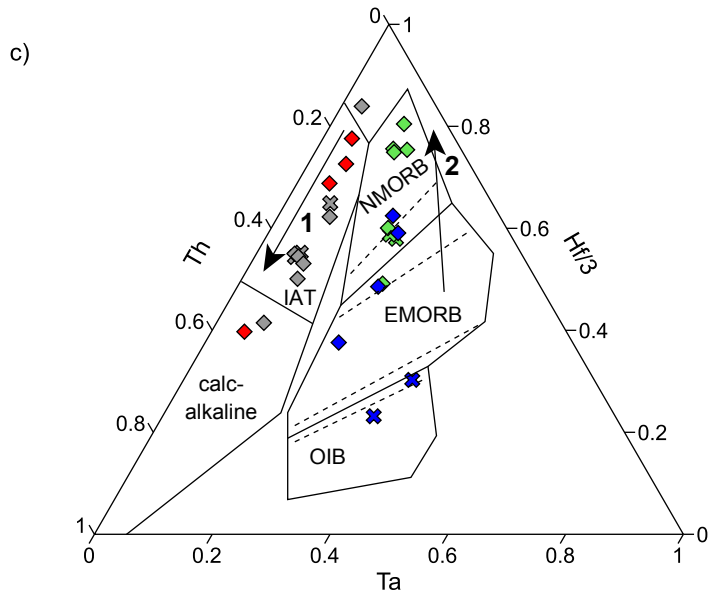
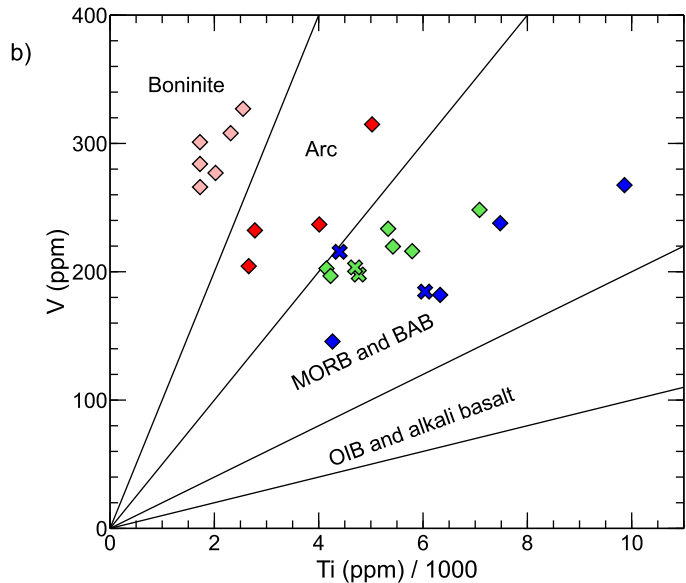
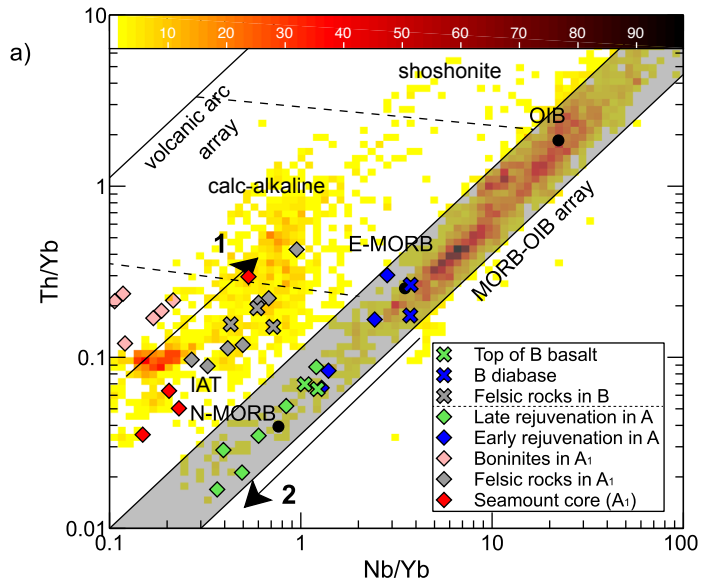
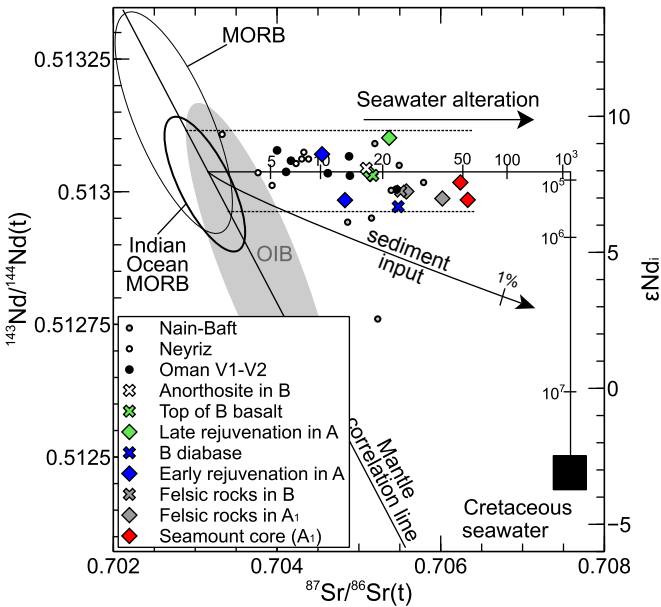
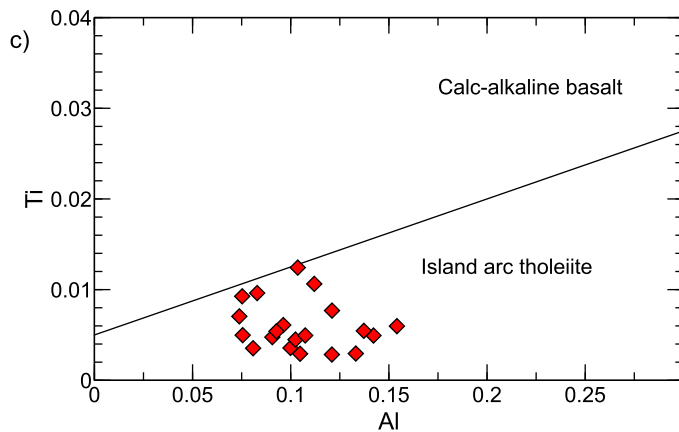
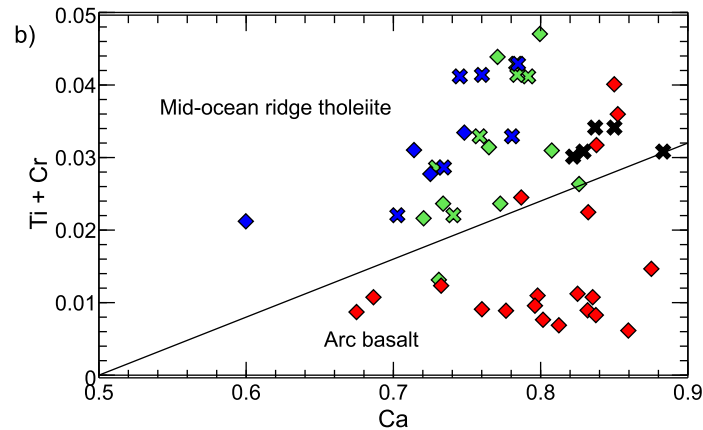
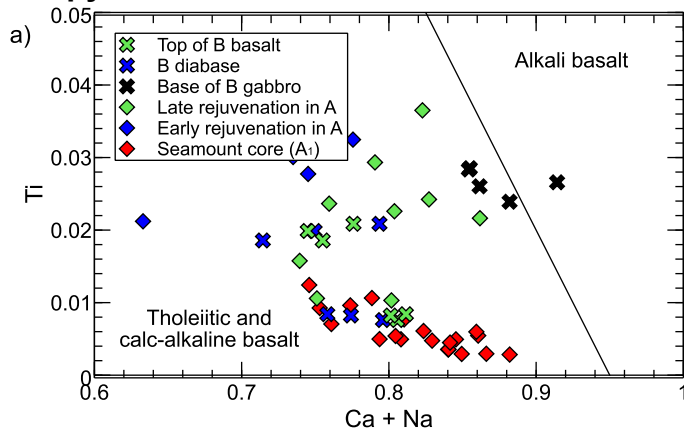


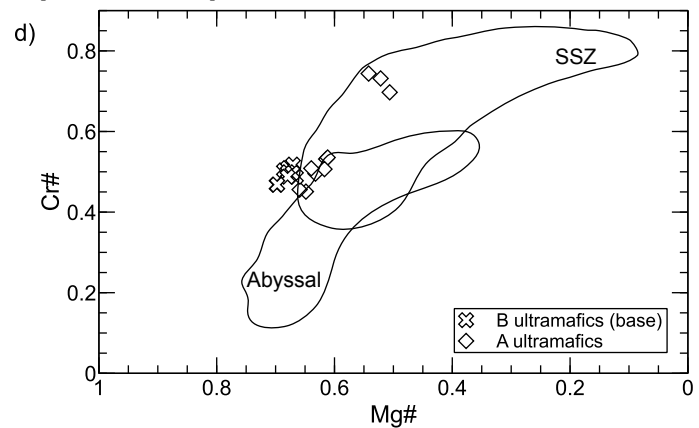
FIG. 8



Clinopyroxene in basaltic rocks



Spinel in serpentinite



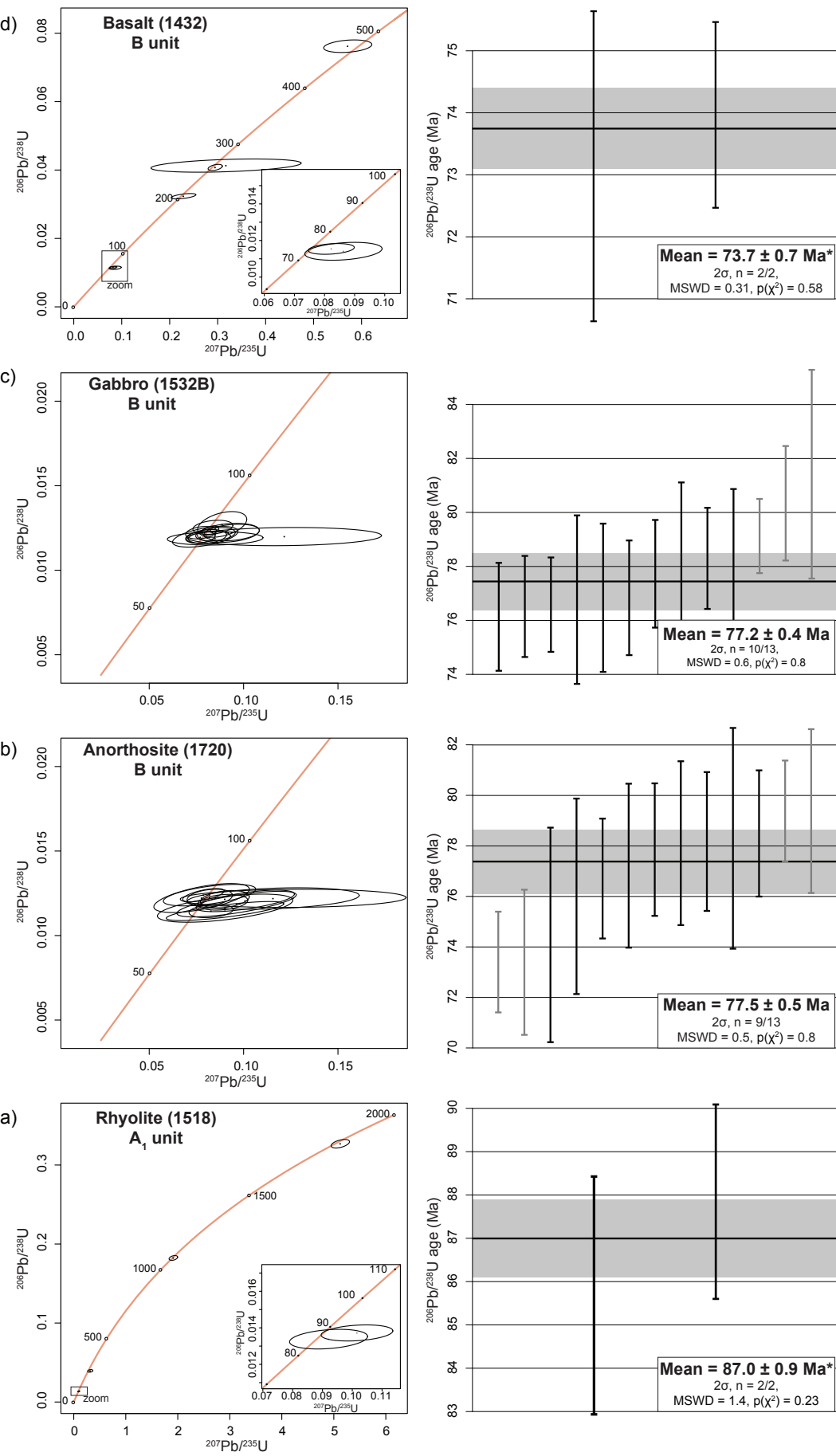
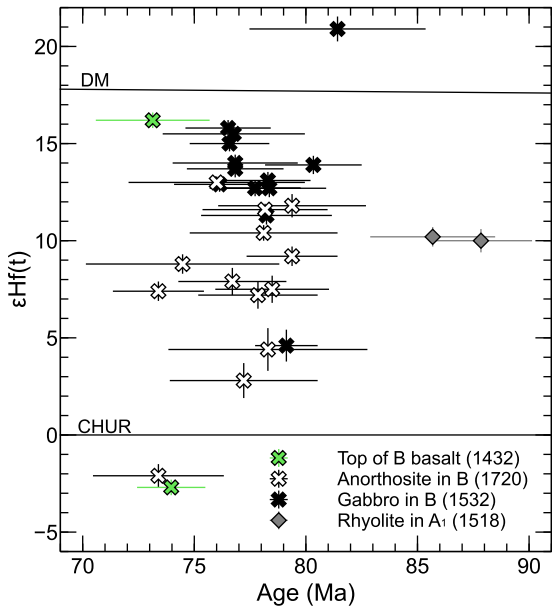
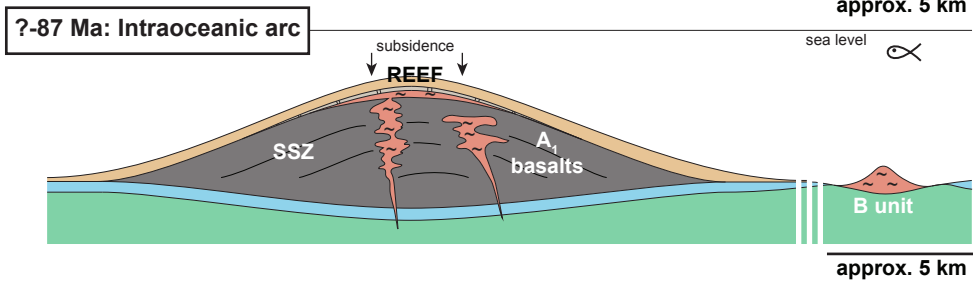
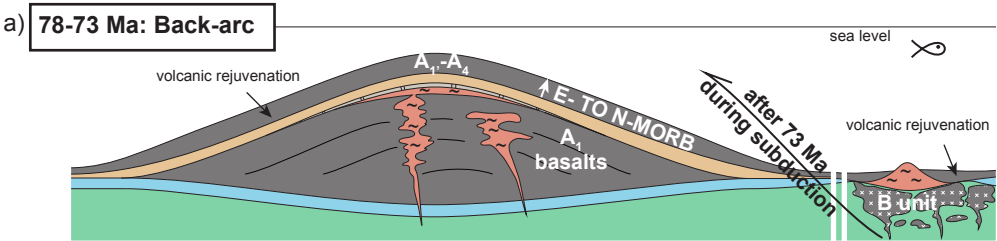
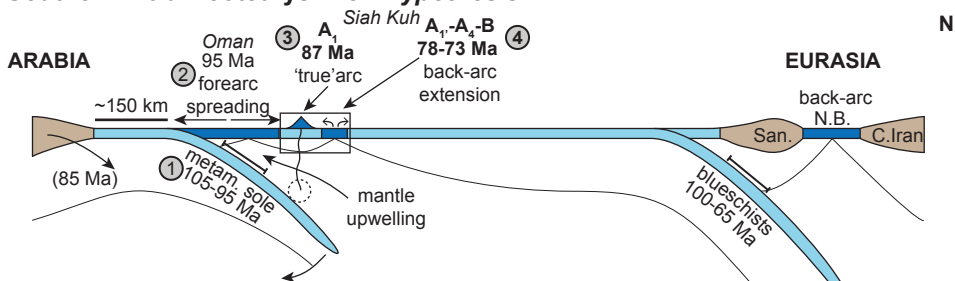


FIG. 11

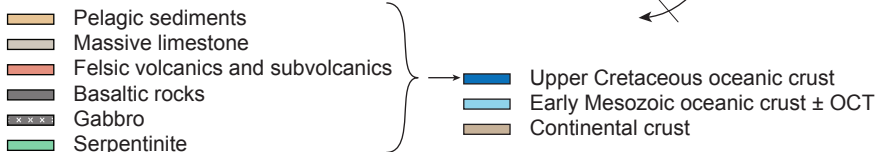
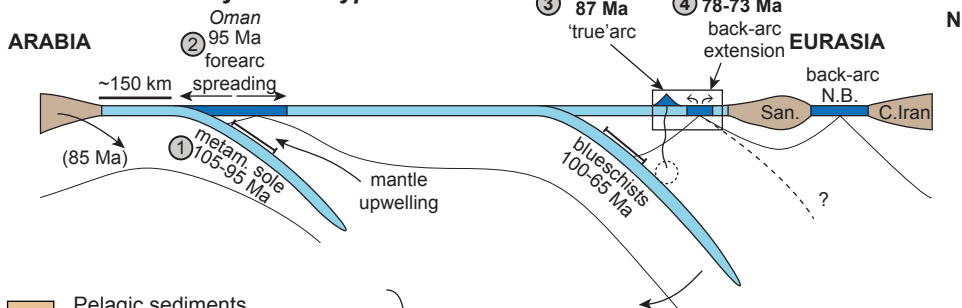




b) **Southern Intra-Neotethys Arc - Hypothesis 1**

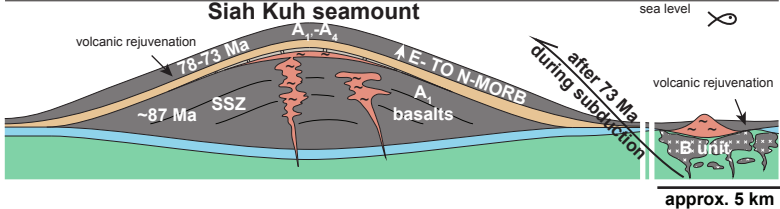


c) **Northern Neotethys Arc - Hypothesis 2**



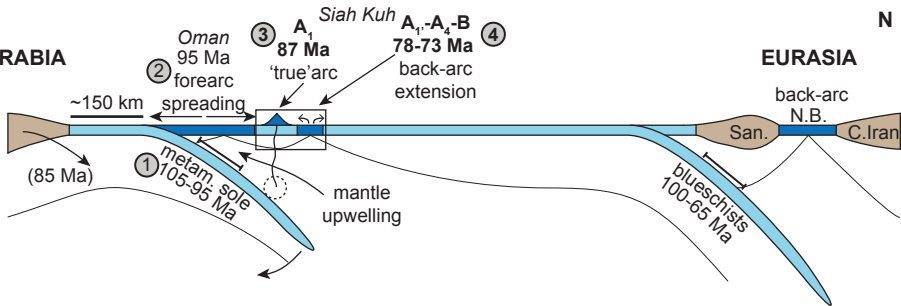
Locality	Type of rock	Age	Possibly represents?	Reference
Kermanshah arc, Western Zagros	Arc volcanism (Kamyaran)	Paleocene-Eocene	2. North Neotethys arc	Whitechurch et al. (2013)
Kermanshah ophiolitic complex (Harsin-Sahneh), Western Zagros	Bisotun carbonates (shallow sediments)	Upper Triassic-Upper Cretaceous	1. rifted allochtons	Ricou (1977); Wrobel-Daveau et al. (2010); Gharib and de Wever (2010)
	Radiolarite series (deep sediments)	Lower Jurassic-"Mid"-Cretaceous		
	Alkaline lavas	Triassic to Liassic	1. rifting	Saccani et al. (2013); Whitechurch et al. (2013)
	IAT	86-81 Ma	3. Cretaceous SSZ magmatism	Whitechurch et al. (2013); Delaloye and Desmons (1980)
	rodingitized gabbro dike in peridotite	79.3	4. Late Cretaceous spreading?	Ao et al. (2016); Wrobel-Daveau et al. (2010)
Zagros eclogites, Western Zagros	Shahrekord eclogite	185-110 Ma	2. North Neotethys subduction?	Davoudian et al. (2008, 2016)
Neyriz ophiolitic complex, Central Zagros	Megalodon limestone (shallow sediments)	Upper-Triassic	1. rifted allochtons	Jannessary and Whitechurch (2008); Ricou (1974)
	Pichakun unit (deep sediments)	Upper Triassic-"Mid"-Cretaceous		
	Alkaline lavas	Triassic	1. rifting	Ricou (1974)
	metamorphic sole	94.9 ± 7.6 Ma	3. South Neotethys subduction	Lanphere and Pamić (1983)
	arc tholeiite to boninites	100-92 Ma	3. Cretaceous SSZ magmatism	Moghadam et al. (2014b); Babaie et al. (2006); Jannessary (2003); Lanphere and Pamić (1983); Monsef et al. (2018a)
	calc-alkaline volcanics (Hassanabad unit)	Cretaceous	3. Cretaceous SSZ magmatism	Babaie et al. (2001)
Siah Kuh unit, Eastern Zagros	Arc tholeiites - core of seamount	before 87 Ma? ... 95 Ma?	3. Cretaceous SSZ magmatism	Moghadam et al. (2013b); this study
	Felsic volcanism	87 Ma?	3. Cretaceous SSZ magmatism	this study
	MORB magmatism	78-73 Ma	4. Late Cretaceous spreading	this study
South Hajiabad ophiolite, Eastern Zagros	E-MORB lavas	194-186 Ma	1. early spreading	Moghadam et al. (2013b); Moghadam et al. (2017)
Zagros blueschists, Eastern Zagros	Ashin blueschists Seghin blueschists	120-60 Ma	2. North Neotethys subduction	Agard et al. (2006); Monié and Agard (2009); Angiboust et al. (2016); Moghadam et al. (2017)
Sikhoran mafic-ultramafic complex, Eastern Zagros	Gabbroic complexes (contaminated MORB)	250 -180 Ma	1. rifting and early spreading	Ghasemi et al. (2002); Ahmadipour et al. (2003)
	diabasic dykes	160-130 Ma	1. early spreading	Ghasemi et al. (2002)
	E-MORB diabasic dikes	81-76 Ma	4. Late Cretaceous spreading	Ghasemi et al. (2002); Ahmadipour et al. (2003)
Sargaz-Abshur complex, Eastern Zagros	unmetamorphosed sediments	~200 Ma	1. rifting (end)	Sabzehei (1974), Ghasemi et al. (2002)
Oman Exotics, Oman	"Oman exotics" carbonates	Up. Permian to "mid"-Cretaceous	1. rifted allochtons	Searle and Graham (1982)
Haybi complex, Oman	Alkaline lavas	Triassic	1. rifting	Searle (1980)
	E-MORB lavas	Triassic	1. early spreading	Searle (1980)
Semail ophiolite, Oman	metamorphic sole	105 - 95±3 Ma	3. South Neotethys subduction	Hacker et al. (1996); Rioux et al. (2016); Soret et al. (2017); Guilmette et al. (2018)
	V2 volcanism (supra-subduction)	96.4-95.5 Ma	3. Cretaceous SSZ magmatism	Alabaster et al. (1982); Godard et al. (2003); Ishikawa et al. (2002, 2005); Rioux et al. (2012, 2013)
	calc-alkaline felsic intrusives	90-85?	3. Cretaceous SSZ magmatism	Gnos and Peters (1993); Lippard et al. (1986); Searle (1980); Briquet et al. (1981); Ichikawa et al. (2005); Lachize et al. (1996); Rollinson (2015)
Oman blueschists	As-Sifah blueschists and eclogites	~80 Ma	3. South Neotethys subduction	El Shazly et al. (2001); Searle et al. (2004); Warren et al. (2005); Warren and Waters (2006); Yamato et al. (2007)
Makran colored mélange	Limestone rafts	Permian to Late Jurassic	1. rifted allochtons	Burg (2018)
	Alkaline and arc volcanism	~130 Ma and 95-75 Ma	3. Cretaceous SSZ magmatism?	Saccanni et al. (2018)
Makran blueschists	blueschists	~100 Ma	2. North Neotethys subduction	Delaloye and Desmons (1980); Hunziker et al. (2017)
Western Iranian Makran	detrital zircons in sediments	~105, 95, 85, 76 Ma	2. North Neotethys arc	Mohammadi et al. (2017)
Nain-Baft ophiolite, Northern Zagros	SSZ volcanic rocks	Early Cretaceous-Paleocene	2. North Neotethys back-arc?	Moghadam et al. (2009); Moghadam et al. (2013a); Pirnia et al. (2019);
Sistan ophiolite, E. Iran	MORB to SSZ volcanic rocks	Albian-Paleocene(-Eocene)	2. North Neotethys back-arc	Babazadeh and de Wever (2004); Zarrinkoub et al. (2012); Tirrul et al. (1983)
Sabzevar ophiolite, E. Iran	SSZ volcanic rocks	Aptian-Paleocene(-Eocene)	2. North Neotethys back-arc	Rossetti et al. (2014), Moghadam et al. (2014a)
Sanandaj-Sirjan zone, Northern Zagros	Arc volcanism	Early Jurassic?-Late Cretaceous	2. North Neotethys arc	Arvin et al. (2007); Shahbazi et al. (2010); Jafari et al. (2018)
Urumieh-Dokhtar zone, Northern Zagros	Arc volcanism	Post-Eocene	2. North Neotethys arc	Omrani et al. (2008)

Siah Kuh seamount



S

ARABIA



N

EURASIA

back-arc
N.B.

San.

C. Iran